

# Finite-time Lyapunov exponents and Lagrangian coherent structures in the infinitesimal integration time limit

Peter J. Nolan · Shane D. Ross

Received: date / Accepted: date

**Abstract** Lagrangian diagnostics, such as the finite-time Lyapunov exponent and Lagrangian coherent structures, have become popular tools for analyzing unsteady fluid flows. These diagnostics can help illuminate regions where particles transported by a flow will converge to and diverge from, even in a divergence-free flow. Unfortunately, calculating Lagrangian diagnostics can be time consuming and computationally expensive. Recently, new Eulerian diagnostics have been developed which provide similar insights into the Lagrangian transport properties of fluid flows. These new diagnostics are faster and less expensive to compute than their Lagrangian counterparts. Because Eulerian diagnostics of Lagrangian transport structure are relatively new, there is still much about their connection to Lagrangian diagnostics that is unknown. This paper provides a mathematical bridge between Lagrangian and Eulerian diagnostics. It rigorously explores the mathematical relationship that exists between invariants of the right Cauchy-Green deformation tensor and the Rivlin-Ericksen tensors, primarily the Eulerian rate-of-strain tensor, in the infinitesimal integration time limit. Additionally, this paper develops the infinitesimal-time Lagrangian coherent structures (iLCSs) and demonstrates their efficacy in predicting the Lagrangian transport of particles even in realistic geophysical fluid flows generated by numerical models.

**Keywords** Lagrangian coherent structures · dynamical systems · Lagrangian transport structure · fluid mechanics · phase space transport · Cauchy-Green deformation tensor · Lyapunov exponents · invariant manifolds · geophysical fluids

---

Peter J. Nolan (Corresponding author) · Shane D. Ross  
Engineering Mechanics Program  
Virginia Tech  
Tel.: +1-540-231-1616  
E-mail: pnolan86@vt.edu

## 1 Introduction

Lagrangian diagnostics, such as the finite-time Lyapunov exponent (FTLE) and Lagrangian coherent structures (LCSs), have become a popular means of analyzing the Lagrangian transport structure of unsteady fluid flows and other dynamical systems [1–34]. These diagnostics predict the dominant particle deformation patterns in a fluid flow over a time interval of interest, as well as which regions of the flow will undergo the greatest and least amounts of stretching. However, Lagrangian methods rely on the numerical integration of particle trajectories, making such methods computationally expensive and time consuming. Furthermore, the integration of particle trajectories requires a velocity field which is sufficiently resolved in both time and space in order to accurately calculate the particle’s motion. This limits the ability of researchers to compute Lagrangian diagnostics from experimental or observational data, such as from particle image velocimetry (PIV) in laboratory-scale experimental fluid mechanics [35–38], biological applications [8, 39–41], such as cardiovascular flows [42–46], or from geophysical data, such as ocean currents [47–50] or wind measurements [51, 52], necessitating the use of simulation-based flow models instead. Additionally, model data takes time to generate, limiting its usefulness for real-time time-critical applications requiring an emergency response [53–55], such as a hazardous incident, e.g., a radioactive material leak [56], an oil spill [57–60], or ocean search-and-rescue [61, 62]. Furthermore, even when model data is readily available it may not be reliable [53, 63–65]. Thus new methods of analyzing unsteady fluid flows are required, which do not depend on particle advection schemes, and could be implemented experimentally in a local spatial neighborhood using only Eulerian information.

Recent Eulerian diagnostics of Lagrangian transport, which do not require integrating particle trajectories, such as objective Eulerian coherent structures which are based on a variational principle [66], the wall shear stress divergence [46], the trajectory divergence rate [67], and the attraction and repulsion rates [51, 68], have been developed to analyze unsteady fluid flows. Most of these diagnostics are derived from the Eulerian rate-of-strain tensor, which is calculated from the gradient of the instantaneous velocity field. This allows for dynamical systems to be analyzed without the need for particle trajectory integration, which reduces the amount of time and computational power necessary to calculate such diagnostics. Furthermore, being based on gradients, these diagnostics can be calculated from measurements using as few as  $n + 1$  points in the neighborhood of a point in  $n$  dimensional space, and at one instant in time. For example, [51] calculated the attraction rate field from experimental two-dimensional environmental fluid measurements using only 3 points in space to estimate the velocity gradient.

This study builds upon the work mentioned above and provides a rigorous foundation connecting the traditional Lagrangian diagnostics and the new Eulerian diagnostics. In particular, the attraction rate is proven to be the limit of the backward-time FTLE as integration time goes to zero, and analogously, the repulsion rate is the limit of the forward-time FTLE as integration

time goes to zero. In addition to this, higher-order Eulerian approximations to the right Cauchy-Green deformation tensor than those currently used are derived—modified Rivlin-Ericksen tensors—expanding in the integration time  $T$ . Using this expansion, high-order approximations are derived for both the backward-time and forward-time FTLE fields, expanding in the integration time  $T$ , and using techniques from matrix perturbation theory. Analytical approximations are derived for the FTLE field for well-known examples, such as the time-varying two-dimensional double-gyre and the three-dimensional ABC flow, which have previously only had their FTLE calculated using numerical particle advection schemes. Examples based on geophysical fluid simulation data are also explored; an atmospheric data set and an oceanic data set. We note that an experimental example has also been considered [51].

Furthermore, a new Eulerian diagnostic tool is introduced—infinitesimal-time Lagrangian coherent structures (iLCSs). The iLCSs are shown to be the limit of LCSs as the integration time  $T$  goes to 0, and are for general  $n$ -dimensional dynamical systems. iLCSs provide a straightforward approach to identifying the major codimension-1 hyperbolic features dominating particle (or general phase space) deformation patterns, as the same ridge detection methods used for the FTLE field can be applied to the attraction and repulsion rate fields. It is demonstrated using analytic and realistic flows that the iLCSs do indeed identify the important cores of particle deformation patterns over short times. Moreover, both attracting and repelling features can be determined simultaneously as they are both based on the instantaneous velocity field gradient—one need not perform two separate particle trajectory integrations, one in forward-time, the other in backward-time. The computational savings in using only the instantaneous velocity field, and not particle trajectory integration, is one of the highlights of the method, making it a candidate for use in real-time applications.

This paper is organized as follows. Section 2 gives information on the dynamical system that will be examined, along with the relevant notation. Section 3 provides a rigorous mathematical connection between invariants of the Eulerian rate-of-strain tensor and traditional Lagrangian diagnostics including the FTLE field. Section 4 derives a new Eulerian diagnostic, iLCSs, as the limit of LCSs as the integration time goes to zero. In section 5, numerous examples are provided, comparing the error of the Eulerian approximation with the benchmark FTLE field (using particle advection algorithms from [69, 70]), demonstrating the effectiveness of iLCSs, and comparing the attraction rate field to the backward-time FTLE field. The attraction rate and backward-time FTLE were focused on due to their usefulness in predicting where particles advected by a flow will converge, making them more relevant to real-world scenarios such as search-and-rescue operations and hazardous release emergencies. Finally, section 6 provides conclusions and future directions.

## 2 Setup and Notation

Consider the dynamical system,

$$\frac{d}{dt}\mathbf{x}(t) = \mathbf{v}(\mathbf{x}(t), t), \quad (1)$$

$$\mathbf{x}_0 = \mathbf{x}(t_0), \quad (2)$$

$$\mathbf{x} \in U \subset \mathbb{R}^n, \quad t \in I \subset \mathbb{R}. \quad (3)$$

This system can be analyzed using Lagrangian (particle trajectory) methods, by first calculating the flow map,  $\mathbf{x}_0 \mapsto \mathbf{x}_t = \mathbf{F}_{t_0}^t(\mathbf{x}_0)$ , for some time interval of interest,  $[t_0, t] \subset I$ , where  $t$  could be greater than or less than the initial time,  $t_0$ . The flow map,  $\mathbf{F}_{t_0}^t : U \rightarrow U$ , is given by,

$$\mathbf{F}_{t_0}^t(\mathbf{x}_0) = \mathbf{x}_0 + \int_{t_0}^t \mathbf{v}(\mathbf{x}(\tau), \tau) d\tau, \quad (4)$$

and is typically given numerically [1, 5, 71, 72]. Taking the gradient of the flow map,  $\nabla \mathbf{F}_{t_0}^t(\mathbf{x}_0)$ , the right Cauchy-Green strain tensor for the time interval of interest can be calculated,

$$\mathbf{C}_{t_0}^t(\mathbf{x}_0) = \nabla \mathbf{F}_{t_0}^t(\mathbf{x}_0)^T \cdot \nabla \mathbf{F}_{t_0}^t(\mathbf{x}_0), \quad (5)$$

which is positive-definite, giving eigenvalues which are all positive and can be ordered as,

$$\lambda_1 \leq \lambda_2 \leq \dots \leq \lambda_n, \quad (6)$$

with associated normalized eigenvectors,

$$\boldsymbol{\xi}_{\lambda_i}, \quad i \in \{1, \dots, n\}. \quad (7)$$

From the maximum eigenvalue of the right Cauchy-Green tensor, the finite-time Lyapunov exponent (FTLE) [1, 2] can be defined as,

$$\sigma_{t_0}^t(\mathbf{x}_0) = \frac{1}{2|T|} \log(\lambda_n), \quad (8)$$

where  $T = t - t_0$  is the (signed) elapsed time, often called the integration time. Recent advances in dynamical systems theory have developed new Eulerian-based methods to analyze the system (1) based on the Eulerian rate-of-strain tensor, defined as,

$$\mathbf{S}(\mathbf{x}, t) = \frac{1}{2} \left( \nabla \mathbf{v}(\mathbf{x}, t) + \nabla \mathbf{v}(\mathbf{x}, t)^T \right), \quad (9)$$

which is symmetric, yielding eigenvalues which are real and can be ordered as,

$$s_1 \leq s_2 \leq \dots \leq s_n, \quad (10)$$

with associated normalized eigenvectors,

$$\boldsymbol{\xi}_{s_i}, \quad i \in \{1, \dots, n\}. \quad (11)$$

From the eigenvalues of the Eulerian rate-of-strain tensor, one can identify regions of the flow which are the most instantaneous attracting and repelling codimension 1 manifolds, as discussed below.

For two-dimensional systems, [66] showed that the minimum eigenvalue,  $s_1$ , provides a measure of instantaneous hyperbolic attraction; with isolated minimas of the  $s_1$  field forming the cores of instantaneous attracting structures they referred to as attracting objective Eulerian coherent structures (OECS). Meanwhile, the maximum eigenvalue,  $s_2$ , was shown to provide a measure of instantaneous hyperbolic repulsion; with isolated maximas of the  $s_2$  field forming the cores of repelling OECS. Furthermore, in [51],  $s_1$  was identified as the attraction rate, with an explicit formula given, and was used to detect attracting LCSs from experimental data. Meanwhile,  $s_2$  was identified as the repulsion rate. This nomenclature will be used in this paper as well, with  $s_n$  replacing  $s_2$  for  $n$ -dimensional systems.

### 3 Expansion of the right Cauchy-Green tensor in the infinitesimal integration time limit

#### 3.1 Eigenvalues of S as FTLE limit as integration time goes to zero

For small  $|T|$ , one can perform a Taylor series expansion of  $\mathbf{C}_{t_0}^t(\mathbf{x})$  in  $T$  as,

$$\mathbf{C}_{t_0}^t(\mathbf{x}) = \mathbb{1} + 2T\mathbf{S}(\mathbf{x}, t_0) + T^2\mathbf{B}(\mathbf{x}, t_0) + \frac{1}{2}T^3\mathbf{Q}(\mathbf{x}, t_0) + \mathcal{O}(T^4), \quad (12)$$

where  $\mathbb{1}$  is the  $n \times n$  identity and where,

$$\mathbf{B}(\mathbf{x}, t_0) \equiv \frac{1}{2} \left[ \nabla \mathbf{a}(\mathbf{x}, t_0) + \nabla \mathbf{a}(\mathbf{x}, t_0)^T \right] + \nabla \mathbf{v}(\mathbf{x}, t_0)^T \cdot \nabla \mathbf{v}(\mathbf{x}, t_0), \quad (13)$$

where the acceleration field,  $\mathbf{a}(\mathbf{x}, t_0)$ , is,

$$\mathbf{a}(\mathbf{x}, t_0) = \frac{d}{dt} \mathbf{v}(\mathbf{x}, t_0) = \frac{\partial}{\partial t} \mathbf{v}(\mathbf{x}, t_0) + \mathbf{v}(\mathbf{x}, t_0) \cdot \nabla \mathbf{v}(\mathbf{x}, t_0), \quad (14)$$

the total time derivative of  $\mathbf{v}(\mathbf{x}, t_0)$ , that is, the acceleration measured along a trajectory (i.e., in a Lagrangian frame). The matrix  $\mathbf{Q}$ , which is dependent on the total time derivative of  $\mathbf{a}(\mathbf{x}, t_0)$ , is given in Appendix A.

Note the following general result for the eigenvalues,

$$\lambda^-(\mathbf{A}) = \lambda_1(\mathbf{A}) \leq \dots \leq \lambda_n(\mathbf{A}) = \lambda^+(\mathbf{A}), \quad (15)$$

of  $n \times n$  real symmetric matrices  $\mathbf{A}$ . For scalar  $c \neq 0$ ,

$$\lambda^\pm(\mathbb{1} + c\mathbf{A}) = 1 + \lambda^\pm(c\mathbf{A}), \quad (16)$$

where,

$$\lambda^\pm(c\mathbf{A}) = \begin{cases} c\lambda^\pm(\mathbf{A}), & \text{for } c > 0, \\ c\lambda^\mp(\mathbf{A}), & \text{for } c < 0. \end{cases} \quad (17)$$

See Appendix B for the proof.

In (8),  $\lambda_n = \lambda^+(\mathbf{C}_{t_0}^t(\mathbf{x}))$ . For small  $T > 0$ , where the  $\mathcal{O}(T^2)$  and higher terms can be neglected,

$$\lambda^+(\mathbf{C}_{t_0}^t(\mathbf{x})) = 1 + 2T\lambda^+(\mathbf{S}(\mathbf{x}, t_0)) + \mathcal{O}(T^2). \quad (18)$$

Thus,

$$\log(\lambda_n) = \log(1 + 2T\lambda^+(\mathbf{S}(\mathbf{x}, t_0))) = 2T\lambda^+(\mathbf{S}(\mathbf{x}, t_0)) = 2Ts_n(\mathbf{x}, t_0), \quad (19)$$

in the limit of small  $T$  using the Taylor expansion,  $\log(1 + \delta) = \delta + \mathcal{O}(\delta^2)$  for small  $|\delta|$ .

From (8), and noting that  $|T| = T$  for  $T > 0$ ,

$$\sigma_{t_0}^t(\mathbf{x}) = \frac{1}{2|T|} \log(\lambda_n) = \frac{1}{2T} 2Ts_n(\mathbf{x}, t_0) = s_n(\mathbf{x}, t_0) \quad (20)$$

Therefore, the maximum eigenvalue of  $\mathbf{S}(\mathbf{x}, t_0)$  is the limit of the FTLE value for forward time as  $T \rightarrow 0^+$ .

For  $T < 0$  with small  $T$ ,

$$\lambda^+(\mathbf{C}_{t_0}^t(\mathbf{x})) = 1 + 2T\lambda^-(\mathbf{S}(\mathbf{x}, t_0)) + \mathcal{O}(T^2). \quad (21)$$

Thus,

$$\log(\lambda_n) = 2T\lambda^-(\mathbf{S}(\mathbf{x}, t_0)) = 2Ts_1(\mathbf{x}, t_0), \quad (22)$$

in the limit of small  $T$ .

From (8), and noting that  $|T| = -T$  for  $T < 0$ ,

$$\sigma_{t_0}^t(\mathbf{x}) = \frac{1}{2|T|} \log(\lambda_n) = -\frac{1}{2T} 2Ts_1(\mathbf{x}, t_0) = -s_1(\mathbf{x}, t_0). \quad (23)$$

Therefore, the negative of the minimum eigenvalue of  $\mathbf{S}(\mathbf{x}, t_0)$  is the limit of the FTLE value for backward time as  $T \rightarrow 0^-$ .

If  $s_1$  and  $s_n$  are denoted as  $s^-$  and  $s^+$ , respectively, the above results can be summarized together as,

$$\sigma_{t_0}^t(\mathbf{x}) = \pm s^\pm(\mathbf{x}, t_0) \quad \text{as } t - t_0 \rightarrow 0^\pm \quad (24)$$

Note that the connection between the proportionality of the eigenvalues of  $\mathbf{S}(\mathbf{x}, t_0)$  and the FTLE for small  $|T|$  was suggested by [73], whereas here the equality in the limit as  $|T| \rightarrow 0$  is proven. Furthermore, in the following section, a means is provided to explicitly write the expansion of the FTLE through any order in  $T$ .

For the  $n = 2$  dimensional case with  $\mathbf{x} = (x, y)$  with the vector field denoted  $\mathbf{v} = (u, v)$ , the velocity gradient tensor is given explicitly as,

$$\nabla \mathbf{v} = \begin{bmatrix} \frac{\partial u}{\partial x} & \frac{\partial u}{\partial y} \\ \frac{\partial v}{\partial x} & \frac{\partial v}{\partial y} \end{bmatrix}, \quad (25)$$

with the Eulerian rate-of-strain tensor,

$$\mathbf{S} = \begin{bmatrix} \frac{\partial u}{\partial x} & \frac{1}{2} \left( \frac{\partial u}{\partial y} + \frac{\partial v}{\partial x} \right) \\ \frac{1}{2} \left( \frac{\partial u}{\partial y} + \frac{\partial v}{\partial x} \right) & \frac{\partial v}{\partial y} \end{bmatrix}. \quad (26)$$

The instantaneous attraction and repulsion rate,  $s^-$  and  $s^+$ , respectively, are then given analytically by,

$$s^\pm(\mathbf{x}, t_0) = \frac{1}{2} \left( \frac{\partial u}{\partial x} + \frac{\partial v}{\partial y} \right) \pm \frac{1}{2} \sqrt{\left( \frac{\partial u}{\partial x} - \frac{\partial v}{\partial y} \right)^2 + \left( \frac{\partial u}{\partial y} + \frac{\partial v}{\partial x} \right)^2}. \quad (27)$$

If  $\mathbf{v}(\mathbf{x})$  represents a two-dimensional fluid velocity, then the attraction and repulsion rates can be written as,

$$s^\pm(\mathbf{x}, t_0) = \frac{1}{2} \operatorname{div}(\mathbf{v}(\mathbf{x}, t_0)) \pm \frac{1}{2} \varepsilon(\mathbf{x}, t_0). \quad (28)$$

in terms of fluid quantities, where,

$$\operatorname{div}(\mathbf{v}(\mathbf{x}, t_0)) = \nabla \cdot \mathbf{v}(\mathbf{x}, t_0) = \frac{\partial u}{\partial x} + \frac{\partial v}{\partial y}, \quad (29)$$

is the divergence of the flow field,  $\varepsilon_N(\mathbf{x}, t_0) = \frac{\partial u}{\partial x} - \frac{\partial v}{\partial y}$  is the normal component of strain,  $\varepsilon_S(\mathbf{x}, t_0) = \frac{\partial u}{\partial y} + \frac{\partial v}{\partial x}$  is the shear component of strain, and,

$$\varepsilon_T(\mathbf{x}, t_0) = \sqrt{\varepsilon_N^2(\mathbf{x}, t_0) + \varepsilon_S^2(\mathbf{x}, t_0)}, \quad (30)$$

is the total strain.

For an incompressible (i.e., divergence-free) two-dimensional flow, notice  $s^\pm(\mathbf{x}, t_0) = \pm \frac{1}{2} \varepsilon_T(\mathbf{x}, t_0)$  and thus,

$$\sigma_{t_0}^t(\mathbf{x}) = \frac{1}{2} \varepsilon_T(\mathbf{x}, t_0), \quad (31)$$

as  $t - t_0 \rightarrow 0$ , that is, both the attracting and repelling fields have the *same structure*, that is, are identical, in the infinitesimal integration time limit.

### 3.2 Approximating FTLE to second-order in integration time

Consider now the third term, the order  $T^2$  term, in the expansion (12) of the right Cauchy-Green tensor. Then (18) becomes,

$$\lambda^+(\mathbf{C}_{t_0}^t(\mathbf{x})) = 1 + 2T\lambda^+(\mathbf{S}(\mathbf{x}, t_0) + \frac{1}{2}T\mathbf{B}(\mathbf{x}, t_0)) + \mathcal{O}(T^3). \quad (32)$$

Note that  $\mathbf{B}(\mathbf{x}, t_0)$ , like  $\mathbf{S}(\mathbf{x}, t_0)$ , is symmetric, i.e.,  $\mathbf{B}(\mathbf{x}, t_0)^T = \mathbf{B}(\mathbf{x}, t_0)$ . It can be shown via matrix perturbation techniques (see Appendix C) that,

$$\lambda^+(\mathbf{S}(\mathbf{x}, t_0) + \frac{1}{2}T\mathbf{B}(\mathbf{x}, t_0)) = s_n + \frac{1}{2}T\boldsymbol{\xi}_{s_n}^T \mathbf{B} \boldsymbol{\xi}_{s_n} + \mathcal{O}(T^2). \quad (33)$$

Using the Taylor expansion  $\log(1 + \delta) = \delta - \frac{1}{2}\delta^2 + \frac{1}{3}\delta^3 + \mathcal{O}(\delta^4)$  for small  $|\delta|$ , by a similar argument as before, for small  $T$ ,

$$\begin{aligned} \log(\lambda^+(\mathbf{C}_{t_0}^t(\mathbf{x}))) &= \log\left(1 + 2T\left[s_n + \frac{1}{2}T\xi_{s_n}^T \mathbf{B}\xi_{s_n} + \mathcal{O}(T^2)\right]\right), \\ &= 2T\left[s_n + \frac{1}{2}T\xi_{s_n}^T \mathbf{B}\xi_{s_n} + \mathcal{O}(T^2)\right] - \frac{1}{2}4T^2s_n^2 + \mathcal{O}(T^3), \quad (34) \\ &= 2T\left[s_n + T\left(-s_n^2 + \frac{1}{2}\xi_{s_n}^T \mathbf{B}\xi_{s_n}\right) + \mathcal{O}(T^2)\right]. \end{aligned}$$

Therefore, for  $T > 0$  with small  $|T|$ ,

$$\sigma_{t_0}^t(\mathbf{x}) = s_n(\mathbf{x}, t_0) + T\left(-s_n(\mathbf{x}, t_0)^2 + \frac{1}{2}\xi_{s_n}(\mathbf{x}, t_0)^T \mathbf{B}(\mathbf{x}, t_0)\xi_{s_n}(\mathbf{x}, t_0)\right) + \mathcal{O}(T^2). \quad (35)$$

And similarly, for  $T < 0$  with small  $|T|$ ,

$$\sigma_{t_0}^t(\mathbf{x}) = -s_1(\mathbf{x}, t_0) - T\left(-s_1(\mathbf{x}, t_0)^2 + \frac{1}{2}\xi_{s_1}(\mathbf{x}, t_0)^T \mathbf{B}(\mathbf{x}, t_0)\xi_{s_1}(\mathbf{x}, t_0)\right) + \mathcal{O}(T^2). \quad (36)$$

If terms through second order in  $T$  are included, then the following is obtained,

$$\begin{aligned} \sigma_{t_0}^t(\mathbf{x}) &= s_n + T\left(-s_n^2 + \frac{1}{2}\mu_1\right) + T^2\left(\frac{4}{3}s_n^3 - s_n\mu_1 + \frac{1}{4}\mu_2\right) + \mathcal{O}(T^3) \text{ for } T > 0, \\ \sigma_{t_0}^t(\mathbf{x}) &= -s_1 - T\left(-s_1^2 + \frac{1}{2}\mu_1\right) - T^2\left(\frac{4}{3}s_1^3 - s_1\mu_1 + \frac{1}{4}\mu_2\right) + \mathcal{O}(T^3) \text{ for } T < 0, \end{aligned} \quad (37)$$

where  $\mu_1$  and  $\mu_2$  are from (97) and (106), respectively, in Appendix C, and the dependence on  $\mathbf{x}$  and  $t_0$  is understood.

### 3.3 Equality of the eigenvectors of $\mathbf{S}$ and $\mathbf{C}$ as integration time goes to zero

Let  $\mathbf{C}$  be the  $n \times n$  right Cauchy-Green strain tensor,  $\mathbf{S}$  the  $n \times n$  Eulerian rate-of-strain tensor,  $\lambda_i$  an ordered eigenvalue of  $\mathbf{C}$ ,  $s_i$  an ordered eigenvalue of  $\mathbf{S}$ , and  $\mathbb{1}$  the  $n \times n$  identity matrix. Let  $T > 0$  be small enough that the relationships in (12) and (18) hold and  $\mathcal{O}(T^2)$  terms are negligible. Assume that  $\xi_i$  is the eigenvector of  $\mathbf{S}$  associated with  $s_i$ , then

$$\mathbf{S}\xi_i = s_i\xi_i, \quad (38)$$

$$2T\mathbf{S}\xi_i + \xi_i = 2Ts_i\xi_i + \xi_i, \quad (39)$$

$$(2T\mathbf{S} + \mathbb{1})\xi_i = (2Ts_i + 1)\xi_i, \quad (40)$$

$$\mathbf{C}\xi_i = \lambda_i\xi_i, \quad (41)$$

where the dependence on  $\mathbf{x}$  and  $t_0$  is understood and we used the order- $T$  approximation for  $\mathbf{C}$ . Thus, if  $\xi_i$  is an eigenvector of  $\mathbf{S}$ , then  $\xi_i$  is an eigenvector of  $\mathbf{C}$ . Now, assuming that  $\xi_i$  is the eigenvector of  $\mathbf{C}$  associated with  $\lambda_i$ , and working through (38-41) in reverse proves that if  $\xi_i$  is an eigenvector of  $\mathbf{C}$ , then  $\xi_i$  is an eigenvector of  $\mathbf{S}$  in the limit as  $T$  goes to 0. For  $T < 0$  an analogous argument holds using (21) in place of (18) and with the ordering of the eigenvalues opposed, i.e.  $\lambda_i \sim s_{n-i+1}$ ,  $i \in [1, n]$ .

Therefore, in the limit as  $|T|$  goes to 0, the eigenvectors of  $\mathbf{S}$  and  $\mathbf{C}$  are equal. For small  $|T|$ , we can also use the perturbation expansion of  $\mathbf{C}$ , to get the estimated eigenvectors of  $\mathbf{C}$  from (88) in Appendix C, which provides the eigenvectors through order  $T^2$  using only the velocity field  $\mathbf{v}$  from (1) evaluated at  $\mathbf{x}$  and time  $t_0$  as well as appropriate derivatives.

#### 4 Infinitesimal-time Lagrangian coherent structures (iLCS)

Previous work [1, 2, 9, 13, 14, 17, 18, 21, 23] has demonstrated that Lagrangian coherent structures (LCSs) can be identified as ridges of the FTLE field. While there are different mathematical definitions for what constitutes a ridge, a co-dimension 1 ridge can be thought of as the generalization of the concept of local maxima. For this study, LCSs will be identified as C-ridges of the FTLE field. C-ridges were first described in [74], as ridges of the FTLE which are orthogonal to the direction of maximal stretching. They are defined as,

$$\sigma > 0, \quad (42)$$

$$\nabla\sigma \cdot \boldsymbol{\xi}_{\lambda_n} = 0, \quad (43)$$

$$(\mathbf{H}_\sigma \cdot \boldsymbol{\xi}_{\lambda_n}) \cdot \boldsymbol{\xi}_{\lambda_n} < 0, \quad (44)$$

where the dependence on  $\mathbf{x}$ ,  $t_0$ , and  $t$  is understood, and  $\mathbf{H}_\sigma$  denotes the Hessian of the FTLE field. C-ridges are advantageous over other definitions of ridges for the FTLE field, as they only rely on invariants of the right Cauchy-Green strain tensor. C-ridges of the FTLE field have also been proven in [74] to be mathematically equivalent to the variational definition of hyperbolic LCSs given in [12].

We propose an instantaneous approximation to the traditional finite-time LCS, called the infinitesimal-time LCS (iLCS). Following [74], we seek co-dimension 1 manifolds in the phase space which maximize local stretching and are orthogonal to the direction of maximal stretching. For a flow  $\mathbf{F}_{t_0}^t$ , the FTLE field provides a measure of stretching over a given time period. As  $-s_1$  and  $s_n$  are the limits of the backward-time and forward-time FTLE fields as integration time goes to 0, we seek ridges of these fields which are orthogonal to the direction of maximal stretching. The direction of maximal stretching in a flow over a time interval is the given by the eigenvector of the right Cauchy-Green strain tensor associated with the largest eigenvalue. As the eigenvectors of the right Cauchy-Green and Eulerian tensors are equal in the infinitesimal-time limit, we seek ridges of  $-s_1$  and  $s_2$  which are orthogonal to their associated eigenvector. Following [74], these ridges will be referred to as S-ridges. S-ridges are thus the limit of C-ridges as integration time goes to zero. Because of this, S-ridges are mathematically equivalent to the variational definition of LCS as the integration time goes to zero.

Because an attracting iLCS is a ridge of  $-s_1$ , it can be defined as a trough of  $s_1$ , as illustrated in Figure 1. Mathematically, this can be expressed as,

$$s_1 < 0, \quad (45)$$

$$\nabla s_1 \cdot \boldsymbol{\xi}_{s_1} = 0, \quad (46)$$

$$(\mathbf{H}_{s_1} \cdot \boldsymbol{\xi}_{s_1}) \cdot \boldsymbol{\xi}_{s_1} > 0. \quad (47)$$

where the dependence on  $\mathbf{x}$ ,  $t_0$ , and  $t$  is understood. Additionally, as a ridge

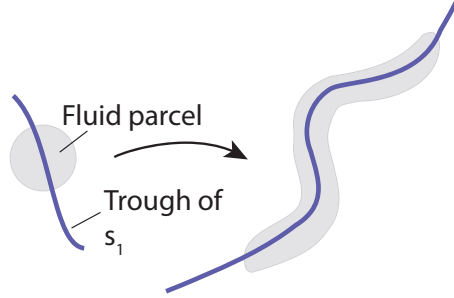


**Fig. 1** Schematic of the effect of a trough of the attraction rate  $s_1$  field on a blob of advected particles, for example, a fluid parcel if the flow is a fluid.

of  $s_n$ , a repelling iLCS can be mathematically expressed as,

$$s_n > 0, \quad (48)$$

$$\nabla s_n \cdot \boldsymbol{\xi}_{s_n} = 0, \quad (49)$$

$$(\mathbf{H}_{s_n} \cdot \boldsymbol{\xi}_{s_n}) \cdot \boldsymbol{\xi}_{s_n} < 0. \quad (50)$$

where, again, the dependence on  $\mathbf{x}$ ,  $t_0$ , and  $t$  is understood.

It should be noted that iLCSs are not restricted to two-dimensional flows, as other Eulerian diagnostics have been, but generalize to  $n$ -dimensional systems. Section 5.1 considers a nonlinear saddle flow which can be worked out entirely analytically. Section 5.2 considers the time-dependent double-gyre, for which the velocity field can be written analytically. Sections 5.3 and 5.4 examine iLCSs in realistic time-dependent two-dimensional geophysical flows. Section 5.5 applies iLCSs to a time-dependent three-dimensional extension of the double-gyre flow. Finally section 5.6 explores the use of iLCSs in a fully coupled three-dimensional flow.

## 5 Examples

### 5.1 Two-Dimensional Nonlinear Saddle Flow

Consider the nonlinear saddle flow,

$$\begin{aligned} \dot{x} &= x, \\ \dot{y} &= -y - y^3. \end{aligned} \quad (51)$$

These two uncoupled ordinary differential equations admit the explicit solutions,

$$\begin{aligned} x(t) &= x_0 e^t, \\ y(t) &= \frac{y_0}{\sqrt{(1+y_0^2)e^{2t} - y_0^2}}, \end{aligned} \quad (52)$$

where the initial condition at time  $t_0 = 0$  is  $\mathbf{x}_0 = (x_0, y_0)$ . While the  $y$  solution goes to infinity in finite integration time, only times small enough to be below the singular limit are considered. The right Cauchy-Green deformation tensor for a small backward integration time  $T < 0$ , is,

$$\mathbf{C}_0^T(\mathbf{x}_0) = \begin{bmatrix} e^{2T} & 0 \\ 0 & \frac{e^{4T}}{((1+y_0^2)e^{2T} - y_0^2)^3} \end{bmatrix}, \quad (53)$$

which yields a backward time FTLE of

$$\sigma_0^T(\mathbf{x}_0) = -\frac{1}{2T} \log \left( \frac{e^{4T}}{((1+y_0^2)e^{2T} - y_0^2)^3} \right). \quad (54)$$

Writing the log term as follows, using a Taylor series approximations for small  $|T|$ ,

$$\begin{aligned} & \log(e^{4T}) - \log[(1+y_0^2)e^{2T} - y_0^2]^3, \\ &= 4T - 3 \log[(1+y_0^2)(1+2T + \frac{1}{2!}(2T)^2 + \frac{1}{3!}(2T)^3 + \mathcal{O}(T^4)) - y_0^2], \\ &= 4T - 3 \log[1 + (1+y_0^2)2T + (1+y_0^2)2T^2 + (1+y_0^2)\frac{4}{3}T^3 + \mathcal{O}(T^4)], \\ &= 4T - 3[(1+y_0^2)2T + (1+y_0^2)2T^2 - \frac{1}{2}(1+y_0^2)^2 4T^2 \\ &\quad + \frac{1}{3}(1+y_0^2)^3(2T)^2 + \frac{4}{3}(1+y_0^2)T^3 - \frac{1}{2}(1+y_0^2)^2(2T)^3 + \mathcal{O}(T^4)], \\ &= 4T - (1+y_0^2)6T + 6T^2 y_0^2(1+y_0^2) - 4y_0^2(1+y_0^2)(1+2y_0^2)T^3 + \mathcal{O}(T^4), \\ &= -2T[(1+3y_0^2) - 3y_0^2(1+y_0^2)T + 2y_0^2(1+y_0^2)(1+2y_0^2)T^2 + \mathcal{O}(T^3)]. \end{aligned} \quad (55)$$

So the FTLE is expanded in  $T$  as follows, obtained by dividing by  $-2T$ ,

$$\sigma_0^T(\mathbf{x}_0) = (1+3y_0^2) - 3y_0^2(1+y_0^2)T + 2y_0^2(1+y_0^2)(1+2y_0^2)T^2 + \mathcal{O}(T^3). \quad (56)$$

The FTLE is now approximated by the first, second, and third terms (the zeroth-order, first-order, and second-order in  $T$ , respectively) using the procedure outlined in section 3.2. The gradient of the velocity is,

$$\nabla \mathbf{v}(\mathbf{x}_0) = \begin{bmatrix} 1 & 0 \\ 0 & -(1+3y_0^2) \end{bmatrix}, \quad (57)$$

which is also  $\mathbf{S}(\mathbf{x}_0)$ , since the gradient is diagonal. This has a minimum eigenvalue  $s_1 = -(1+3y_0^2)$ , the negative of which matches the first term of (56),

as prescribed by (36). To calculate the second term of (56), the term first-order in  $T$ , the acceleration field needs to be calculated and then  $\mathbf{B}(\mathbf{x}_0)$ . The acceleration field is, following (14),

$$\begin{aligned}\ddot{x} &= \frac{d}{dt}\dot{x} = x, \\ \ddot{y} &= \frac{d}{dt}\dot{y} = y + 4y^3 + 3y^5.\end{aligned}\tag{58}$$

Therefore (13) gives,

$$\begin{aligned}\mathbf{B}(\mathbf{x}_0) &= \begin{bmatrix} 1 & 0 \\ 0 & (1 + 12y_0^2 + 15y_0^4) \end{bmatrix} + \begin{bmatrix} 1 & 0 \\ 0 & (1 + 6y_0^2 + 9y_0^4) \end{bmatrix}, \\ &= \begin{bmatrix} 2 & 0 \\ 0 & (2 + 18y_0^2 + 24y_0^4) \end{bmatrix}.\end{aligned}\tag{59}$$

The normalized eigenvector of  $\mathbf{S}(\mathbf{x}_0)$  corresponding to  $s_1$  is simply  $\boldsymbol{\xi}_0 = [0, 1]^T$ , which via (97) yields,

$$\begin{aligned}\frac{1}{2}\lambda_1 &= \frac{1}{2}\boldsymbol{\xi}_0^T \mathbf{B}(\mathbf{x}_0)\boldsymbol{\xi}_0 = \frac{1}{2} [0 \ 1] \begin{bmatrix} 2 & 0 \\ 0 & (2 + 18y_0^2 + 24y_0^4) \end{bmatrix} \begin{bmatrix} 0 \\ 1 \end{bmatrix}, \\ &= \frac{1}{2}(2 + 18y_0^2 + 24y_0^4), \\ &= 1 + 9y_0^2 + 12y_0^4,\end{aligned}\tag{60}$$

hence,

$$\begin{aligned}-s_1^2 + \frac{1}{2}\boldsymbol{\xi}_0^T \mathbf{B}(\mathbf{x}_0)\boldsymbol{\xi}_0 &= -(1 + 6y_0^2 + 9y_0^4) + 1 + 9y_0^2 + 12y_0^4, \\ &= 3y_0^2 + 3y_0^4, \\ &= 3y_0^2(1 + y_0^2),\end{aligned}\tag{61}$$

the negative of which matches the  $T$  coefficient of the second term of (56), as prescribed by (36).

For the term second-order in  $T$ , note that, as prescribed by (84),

$$\mathbf{Q}(\mathbf{x}_0) = \begin{bmatrix} \frac{8}{3} & 0 \\ 0 & -(\frac{8}{3} + 56y_0^2 + 192y_0^4 + 160y_0^6) \end{bmatrix},\tag{62}$$

and since (102) implies that  $\boldsymbol{\xi}_1$  is parallel to  $\boldsymbol{\xi}_0$ , (106) yields,

$$\lambda_2 = \boldsymbol{\xi}_0^T \mathbf{Q}(\mathbf{x}_0)\boldsymbol{\xi}_0 = -(\frac{8}{3} + 56y_0^2 + 192y_0^4 + 160y_0^6).\tag{63}$$

According to (37), the second-order term is,

$$\begin{aligned}-T^2[\frac{4}{3}s_1^3 - s_1\lambda_1 + \frac{1}{4}\lambda_2] &= -T^2[(-\frac{4}{3} + 2 - \frac{2}{3}) + (-12 + 24 - 14)y_0^2 \\ &\quad + (-36 + 78 - 48)y_0^4 + (-36 + 72 - 40)y_0^6], \\ &= -T^2[0 - 2y_0^2 - 6y_0^4 - 4y_0^6], \\ &= 2y_0^2(1 + y_0^2)(1 + 2y_0^2)T^2,\end{aligned}\tag{64}$$

which matches the  $T^2$  term of the true FTLE field (56).

Thus the formulas of sections 3.1 and 3.2 for approximating the true FTLE, (56), of the nonlinear saddle, (51), through second-order in the integration time  $T$  are verified for this example.

To illustrate the accuracy of the successive approximations, Figure 2 shows the root mean-squared error (RMSE) for the FTLE field as a function of integration time magnitude,  $|T|$ , over the domain  $U = \{(x_0, y_0) \in \mathbb{R}^2 \mid |y_0| < \frac{1}{2}\}$ . Notice that, as expected, the error grows linear in  $|T|$ , quadratic in  $|T|$ , and cubic in  $|T|$ , for the zeroth-order, first-order, and second-order approximations, respectively.

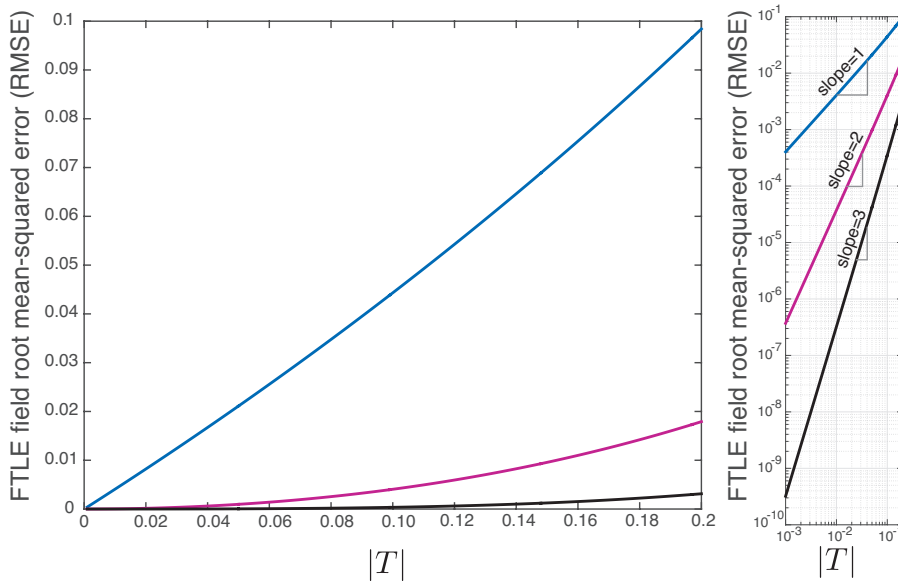


**Fig. 2** Root mean-squared error (RMSE) for successive approximations of the backward-time FTLE field for the nonlinear saddle (51) expanded in  $T$ : zeroth-order (blue), first-order (magenta), second-order (black). Notice that the error grows linear in  $|T|$ , quadratic in  $|T|$ , and cubic in  $|T|$ , respectively, as shown more clearly in the log-log plot on the right.

## 5.2 Two-Dimensional Time-Varying Double-Gyre Flow

While the time-varying double-gyre does not admit an explicit solution, as the previous example does, one can still analytically approximate the FTLE field up to first-order in  $T$  using the formulas of Section 3.2.

Consider the double-gyre flow as described in [1]. This flow comes from the Hamiltonian stream function,

$$\psi(x, y, t) = A \sin(\pi f(x, t)) \sin(\pi y), \quad (65)$$

where,

$$f(x, t) = \epsilon \sin(\omega t)x^2 + (1 - 2\epsilon \sin(\omega t))x. \quad (66)$$

The velocity field,  $\mathbf{v} = (u, v)$ , can be calculate as,

$$\begin{aligned} \dot{x} = u(x, y, t) &= -\frac{\partial \psi}{\partial y} = -A\pi \sin(\pi f(x, t)) \cos(\pi y), \\ \dot{y} = v(x, y, t) &= \frac{\partial \psi}{\partial x} = A\pi \cos(\pi f(x, t)) \sin(\pi y) \frac{\partial f}{\partial x}(x, t). \end{aligned} \quad (67)$$

The domain for  $(x, y)$  is  $U = [0, 2] \times [0, 1]$ . Following [1], parameters  $A = 0.1$ ,  $\omega = 0.2\pi$ , and  $\epsilon = 0.25$  were chosen. The gradient tensor is,

$$\begin{aligned} \nabla \mathbf{v} &= \begin{bmatrix} \frac{\partial u}{\partial x} & \frac{\partial u}{\partial y} \\ \frac{\partial v}{\partial x} & \frac{\partial v}{\partial y} \end{bmatrix}, \\ &= \begin{bmatrix} -\pi^2 A \cos(\pi f) \cos(\pi y) \frac{\partial f}{\partial x} & \pi^2 A \sin(\pi f) \sin(\pi y) \\ -\pi^2 A \sin(\pi f) \sin(\pi y) \frac{\partial f}{\partial x} + \pi A \cos(\pi f) \sin(\pi y) \frac{\partial^2 f}{\partial x^2} & \pi^2 A \cos(\pi f) \cos(\pi y) \frac{\partial f}{\partial x} \end{bmatrix}. \end{aligned} \quad (68)$$

From this gradient, it can be analytically calculated via (27) that the zeroth order approximation to the backward-time FTLE for an initial condition  $\mathbf{x}_0 = (x_0, y_0)$  at initial time  $t_0$  in the infinitesimal integration time limit is,

$$\begin{aligned} s_1 &= -\frac{1}{2} \pi^2 A \left[ \left( \sin(\pi f) \sin(\pi y_0) \left( 1 - \frac{\partial f}{\partial x} \right) + \frac{1}{\pi} \cos(\pi f) \sin(\pi y_0) \frac{\partial^2 f}{\partial x^2} \right)^2 \right. \\ &\quad \left. + 4 \left( \cos(\pi f) \cos(\pi y_0) \frac{\partial f}{\partial x} \right)^2 \right]^{1/2}. \end{aligned} \quad (69)$$

where the dependence of  $s_1$  and  $f$  on  $(\mathbf{x}_0, t_0)$  is understood. This can also be written as,

$$\begin{aligned} s_1 &= -\pi^2 A \left[ \epsilon^2 \sin^2(\omega t) \left\{ \sin^2(\pi y_0) \left( \sin^2(\pi f)(1-x)^2 + \frac{1}{\pi} \sin(2\pi f)(1-x) \right. \right. \right. \\ &\quad \left. \left. + \frac{1}{\pi^2} \cos^2(\pi f) \right) + \cos^2(\pi y_0) \cos^2(\pi f)(1-x)^2 \right\} \\ &\quad \left. + \cos^2(\pi y_0) \cos^2(\pi f) \left( 1 - 4\epsilon \sin(\omega t)(1-x) \right) \right]^{1/2}. \end{aligned} \quad (70)$$

Note that the  $s_1$  field, just like the vector field, is a periodic function of  $t_0$  with period  $2\pi/\omega$ . Note that for  $t_0 = k2\pi/\omega$ , for some integer  $k$ , we have,

$$s_1(x_0, y_0, t_0) = -\pi^2 A |\cos(\pi x_0) \cos(\pi y_0)|. \quad (71)$$

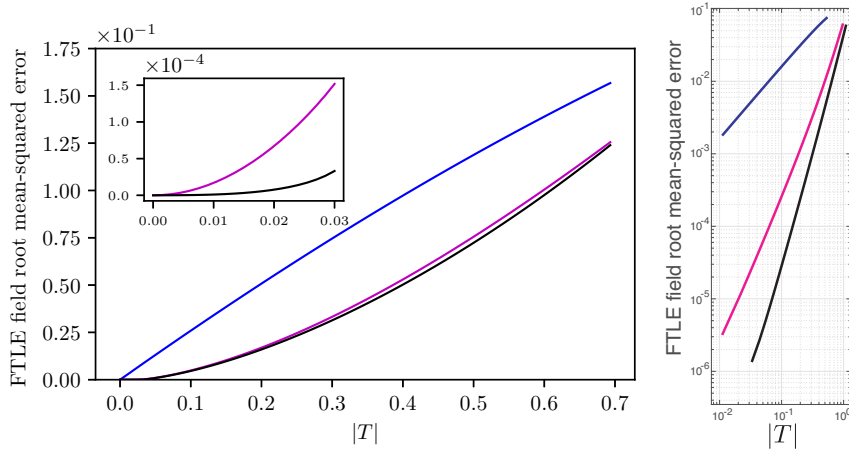


**Fig. 3** Root mean-squared error (RMSE) vs.  $|T|$  for successive approximations of the backward-time FTLE field for the double-gyre flow expanded in  $T$ : zeroth-order (blue), first-order (magenta), second-order (black), showing the error growing linear, quadratic, and cubic in  $|T|$ , respectively, as revealed more clearly in a log-log plot (right).

The first-order term in the backward integration time  $T < 0$  can also be analytically determined. See Appendix D for details.

Figure 3 shows the root-mean-square error between the backward-time FTLE field and the zeroth order (blue), first order (magenta), and second order (black) approximations. In this figure, one can see that as the integration time,  $|T|$ , goes to 0, the approximations converge to the true (benchmark) FTLE field, as is expected. Note that the second-order term is more sensitive to numerical errors than either the zeroth- or first-order terms. Figure 4 shows a

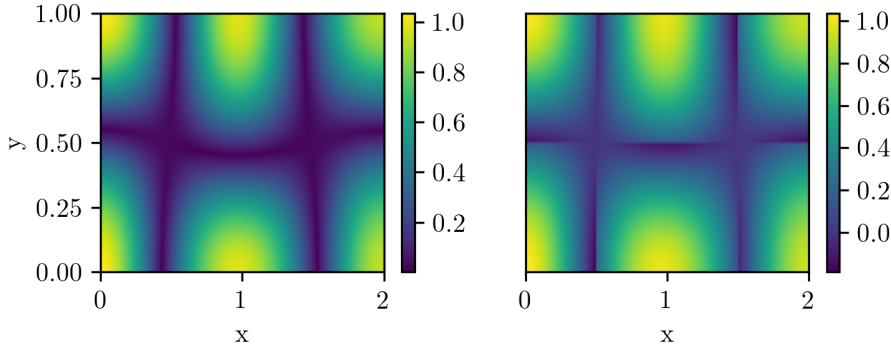


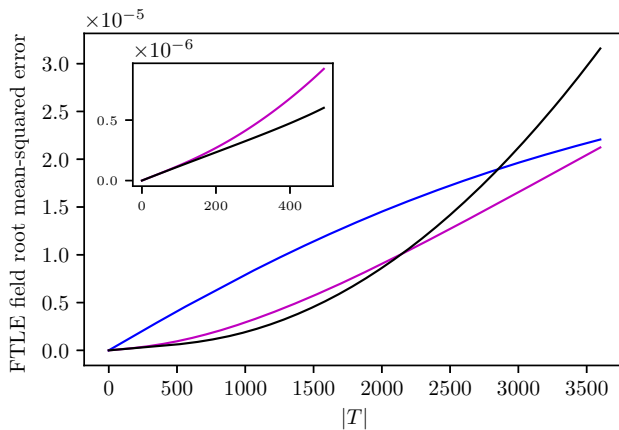
**Fig. 4** Left: True backward-time FTLE field for the double-gyre flow for an integration period of  $T = -0.3$ . Right: The approximation to the FTLE field to first-order in  $T$  for the same integration time  $T = -0.3$ . The root mean-squared error between these two fields is around 0.03 (see figure 3). Parameters:  $A = 0.1$ ,  $\omega = 0.2\pi$ ,  $\epsilon = 0.25$ , and  $t_0 = 0$ .

comparison of the FTLE field for a short integration time,  $T = -0.3$  (center), with an approximation to first order in  $T$  (left).

### 5.3 Two-Dimensional Atmospheric Flow Example

In this section, the methods described above are applied to a realistic time-varying atmospheric flow example, using wind data from a Weather Research and Forecasting (WRF) model simulation over the southeastern United States [75]. This model was run with a horizontal grid resolution of 12 km and temporal resolution of 1 hr. Due to the scale mismatch between the horizontal resolution and the vertical resolution (which varies between 0.05 and 1 km), a single vertical level was chosen to focus on for this analysis. The level that was chosen corresponds to approximately 100 m above ground level (AGL), similar to what has been done in previous atmospheric LCS studies [13, 18, 21, 76], as this is a level reachable by unmanned aerial vehicles for in situ meteorological measurements and sampling [51, 77]. The simulation was performed for a 24 hr period beginning at 0000 UTC 1 July 2011.

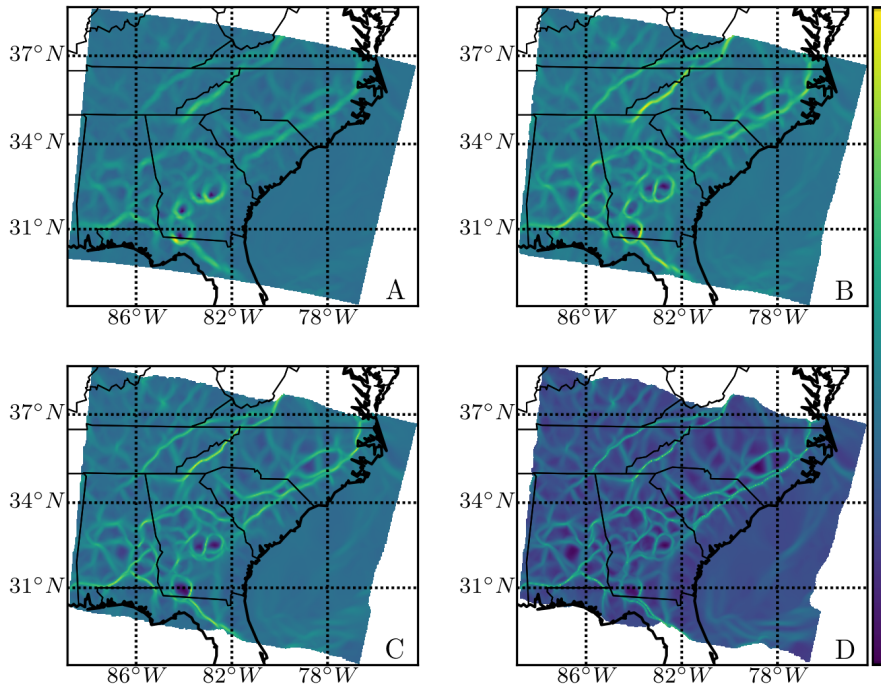
Using this data set the relationship between the attraction rate, higher-order instantaneous approximations, and the backward-time FTLE field for a two-dimensional atmospheric fluid flow can be numerically verified. This can be seen in Figure 5, which shows the RMSE of these approximations with the FTLE field as integration is performed backward in time from 1200 UTC 1 July 2011. The blue line shows the RMSE for the attraction rate, the magenta for the attraction rate with the correction term to first-order in  $T$ , and the black for the attraction rate with the correction term to second-order in  $T$ . As  $|T|$  goes to 0, the RMSE of all three approximations also goes to 0, thus nu-



**Fig. 5** RMSE for successive approximations of the backward-time FTLE field for an atmospheric flow expanded in  $T$ : zeroth-order (blue), first-order (magenta), and second-order (black). Time is in seconds. The inset shows the behavior for the higher order terms for  $|T|$  close to 0.

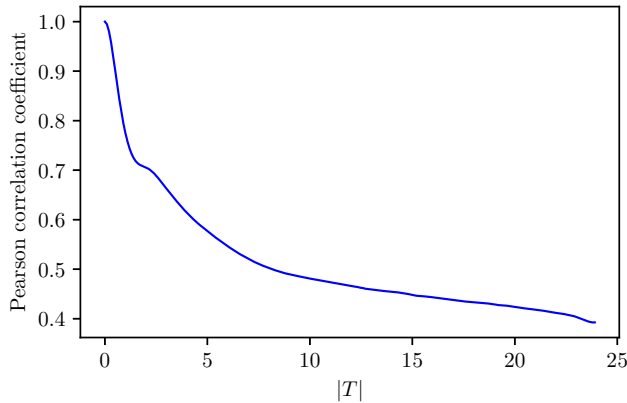
merically verifying the relationships shown in section 3.1 for a two-dimensional atmospheric flow. This figure also shows that for small  $|T|$ , the second-order approximation is the most accurate, as expected. However, for larger  $|T|$  the attraction rate will provide the most accurate approximation, which is to be expected because of the unsteadiness of this flow field. The expansion procedure described in section 3 is based on the instantaneous velocity field (and its gradients) and thus tacitly assumes a time-independent (frozen) flow.

Figure 6 visually explores the connection between the attraction rate and the FTLE field. Panel A shows the attraction rate field at 0000 UTC on 2 July 2011. Panels B, C, and D show the FTLE field after 1, 2, and 4 hours of backward-time integration. In these plots it can be seen that the important Lagrangian transport structures over the period examined are already present in the attraction rate field, even though this accuracy is not reflected in the RMSE plot, Figure 5. As the field is integrated backward in time the transport structures become sharper and grow longer, but do not change significantly. For this particular flow, as the integration time is increased the transport



**Fig. 6** Comparison of the attraction rate (A), with FTLE fields of integration times  $T =$  (B)  $-1$  hr (C)  $-2$  hr, (D)  $-4$  hr. As the integration time increases increases the average FTLE values decreases, thus the comparing the values of the heat-map is less meaningful than comparing the topography. For a topographical analysis, relatively high FTLE values are show in yellow and relatively low values in dark blue (a relative scale color bar is show on the right). The spatial correlation between these fields can is given in Figure 7.

patterns which are shown by the attraction rate field become more sharply defined. This relationship can be quantified by the Pearson correlation coefficient, given in Figure 7, which shows that for short integration times ( $< 4$  hours), there is a strong correlation ( $> 0.6$ ) between the attraction rate and backward-time FTLE field. Then, as the integration time is increased the correlation between the fields becomes weaker. However, note that even after 24 hours, there is still a moderate correlation ( $> 0.4$ ), not yet nearing zero.



**Fig. 7** Pearson correlation coefficient between the attraction rate field and the benchmark backward-time FTLE field as a function of integration time,  $|T|$ , in hours.

This data set allows us to test whether iLCSs are effective at predicting the Lagrangian behavior of passive tracer particles advected in a two-dimensional atmospheric flow, even though they are only evaluated at an initial time,  $t_0 = 0000$  UTC 1 July 2011. Figure 8 shows the evolution of attracting iLCSs (blue), repelling iLCSs (red), and some example passive tracers (cyan). These structures were initialized at  $t_0$  and advected forward in time. Panel A shows the iLCSs and tracers at the initial time. Panels B, C, and D show the iLCSs and tracers after 2, 4, and 8 hours, respectively. An animation of the evolution of the iLCSs and tracers over the entire 24 hr period can be found at <https://youtu.be/h4UhJT8vsiU>. In these panels it can be seen that as time marches forward passive tracers are repelled away from the repelling iLCSs and attracted towards the attracting iLCSs, as expected.

Interestingly, it can also be seen that some of the repelling iLCSs are attracted onto and effectively consumed by the attracting iLCSs. A partial explanation for this can be found in Figure 9, where a comparison between the attraction rate and the repulsion rate fields is shown. Note that the two-dimensional vector field on this level is not divergence-free, as the ignored vertical velocity is non-zero. Thus, the two fields are different (recall they would be the same if the vector field was divergence-free, according to (31)). In this figure, it can be seen that the attraction rate field is stronger than the repulsion rate field is; that is, the most attractive points of the attraction

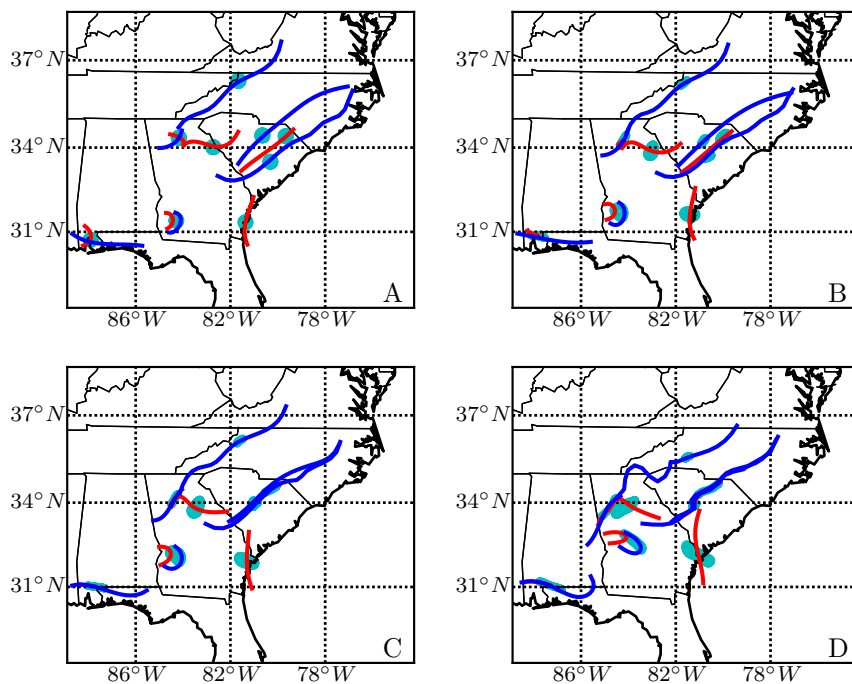


**Fig. 8** iLCSs and passive tracers at different elapsed times,  $t$ , since the initial evaluation time,  $t_0 = 0000$  UTC 1 July 2011, of the simulation. A)  $t - t_0 = 0$  hr, B)  $t - t_0 = 2$  hr, C)  $t - t_0 = 4$  hr, D)  $t - t_0 = 8$  hr. Repelling iLCSs are shown in red, attracting iLCSs in blue, and passive tracers in cyan. An animation of the evolution of the iLCSs and tracers over the entire 24 hr period can be found at <https://youtu.be/h4UhJT8vsiU>.

rate field are more than twice as attractive as the most repelling points in the repulsion rate field are repulsive. Thus, it can be concluded that while the

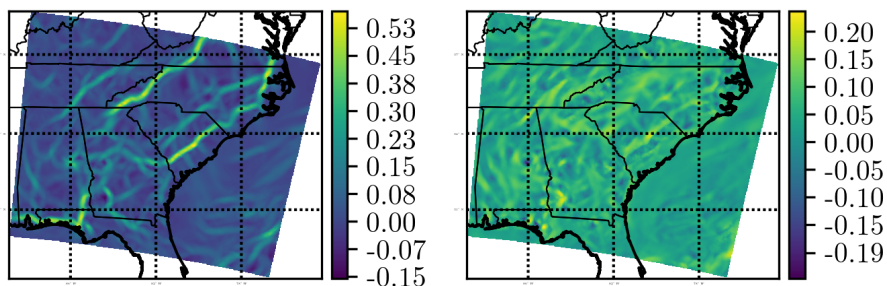


**Fig. 9** Comparison of the attraction rate field,  $s_1$ , left, and the repulsion rate field,  $s_2$ , right, at  $T = 0$ . Structures in the attraction rate field are noticeably stronger than in the repulsion rate field. The attraction rate field has been multiplied by  $-1$  to aid in visualization. The colorbar has units of  $\text{hr}^{-1}$ .

repelling iLCSs are repulsive, the attracting iLCSs are more attractive and thus overpower the repelling iLCSs after a sufficient period of time.

#### 5.4 Two-Dimensional Oceanic Flow Example

In this section, a realistic oceanic flow model is employed to explore the methods described above, using ocean surface velocity data from a Multidisciplinary Simulation, Estimation, and Assimilation Systems (MSEAS) [78] model simulation for the Atlantic Ocean in the vicinity of Martha's Vineyard, Massachusetts. This model was run with a horizontal grid resolution of 200 m and temporal resolution of 1 hr. The fluid simulation forecast was performed for a 24 hour period beginning at 0000 UTC 17 August 2017.

Figure 10 visually explores the connection between the attraction rate and the FTLE field in a two-dimensional oceanic flow. Panel A shows the attraction

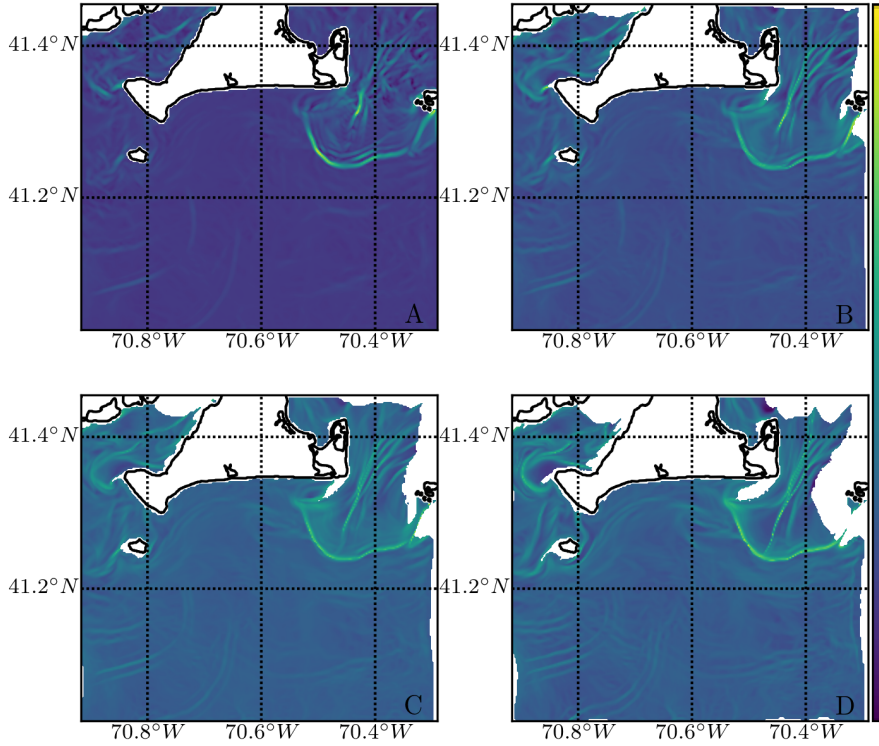


**Fig. 10** Comparison of the attraction rate (A), with FTLE fields of integration times  $T =$  (B)  $-1$  hr (C)  $-2$  hr, (D)  $-4$  hr. As the integration time magnitude increases increases, the average FTLE values decreases, thus comparing the exact values of the heat-map is less meaningful than comparing the topography. For a topographical analysis, relatively high values are show in yellow and relatively low values in dark blue. A relative scale color bar is show on the right. The spatial correlation between these fields can be seen in figure 11.

rate field at  $t_0 = 0000$  UTC 18 August 2017. Panels B, C, and D show the FTLE field for 1, 2, and 4 hours of backward-time integration, initialized at time  $t_0$ . As in the previous section, it can be seen that the significant Lagrangian transport structures over the time interval examined are already present in the attraction rate field. As the field is integrated backward in time the transport structures become sharper and grow longer, but do not change significantly. As in the atmospheric example, as the integration time is increased the transport patterns which are shown by the attraction rate field become more sharply defined. This relationship can be quantified by the Pearson correlation coefficient, which is given in Figure 11. This figure shows that for short integration times ( $< 1.5$  hours), there is a strong correlation ( $> 0.6$ ) between the attraction rate and backward-time FTLE field. Then, as the integration time is increased the correlation between the fields becomes weaker; falling to a weak correlation ( $\sim 0.2$ ) after only 6 hours. The correlation coefficient for this flow drops off more quickly than the in the atmospheric example due to the shorter time-scale of unsteadiness for this flow.

This data set was also able to numerically verify the relationship between the attraction rate, higher-order instantaneous approximations, and the backward-time FTLE field for a two-dimensional oceanic fluid flow. This result is presented in Figure 12, which shows the RMSE of these approximations compared with a benchmark FTLE field, where integration is performed backward in time from  $t_0 = 1200$  UTC 17 August 2017. The blue line shows the RMSE for the attraction rate, the magenta for the attraction rate with a first-order correction term, and the black for the attraction rate with a second-order correction. As  $|T|$  goes to 0, the RMSE of all three approximations also goes to 0, thus numerically verifying the relationships in section 3.1 applied to a two-dimensional oceanic flow.

For this flow, it was further possible to verify that iLCSs are effective at predicting the Lagrangian behavior of passive tracer particles advected in

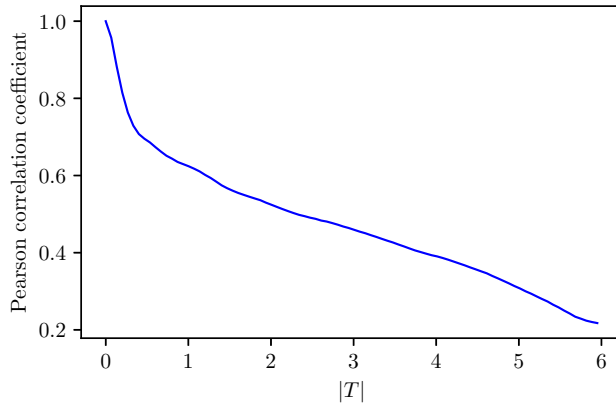


**Fig. 11** Pearson correlation coefficient between the attraction rate field and the benchmark backward-time FTLE field as a function of integration time,  $|T|$ , in hours.

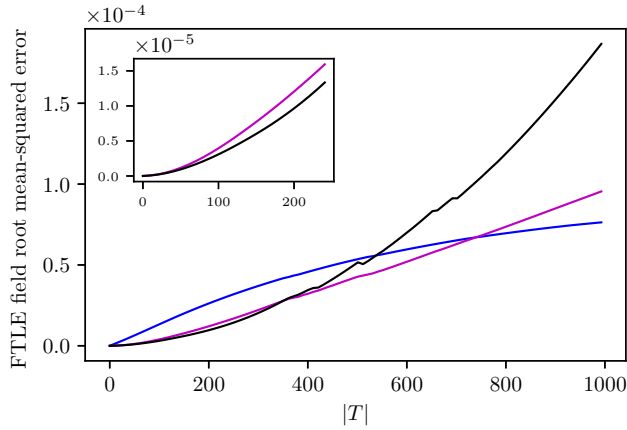


**Fig. 12** RMSE for successive approximations of the backward-time FTLE field for an oceanic flow expanded in  $T$ : zeroth-order (blue), first-order (magenta), and second-order (black). Time is in seconds. The inset shows the behavior for the higher order terms for  $|T|$  close to 0.

a two-dimensional oceanic flow. Figure 13 shows the evolution of attracting iLCSs (blue), repelling iLCSs (red), and some passive tracers (cyan). These structures were initialized at  $t_0 = 0000$  UTC 17 August 2017 and advected forward in time. Panel A shows the iLCSs and tracers at the initial time. Panels B, C, and D show the iLCSs and tracers after 0.5, 1, and 2 hours, respectively. In these panels, one can see that as time moves forward passive tracers are repelled away from the repelling iLCSs and attracted towards the attracting iLCSs, as is expected.

### 5.5 Three-Dimensional Time-Varying Double-Gyre Flow

In this section, iLCSs are applied to a time-dependent three-dimensional flow and the convergence of the attraction rate and higher order approximation to the backward-time FTLE field is further demonstrated. For this section, the time-dependent double-gyre from section 5.2 was extended to 3 dimensions. The new three-dimensional equations are,

$$\dot{x} = -A\pi \sin(\pi f(x, t)) \cos(\pi y), \quad (72)$$

$$\dot{y} = A\pi \cos(\pi f(x, t)) \sin(\pi y) \frac{\partial f}{\partial x}(x, t), \quad (73)$$

$$\dot{z} = 0. \quad (74)$$

with the parameters and function  $f(x, t)$  as defined previously in section 5.2. The domain for  $(x, y, z)$  is  $U = [0, 2] \times [0, 1] \times [0, 1]$ . While this flow is trivially three-dimensional (i.e., there is no motion in the vertical direction), it does serve as a proof of concept that iLCSs work for three-dimensional systems.

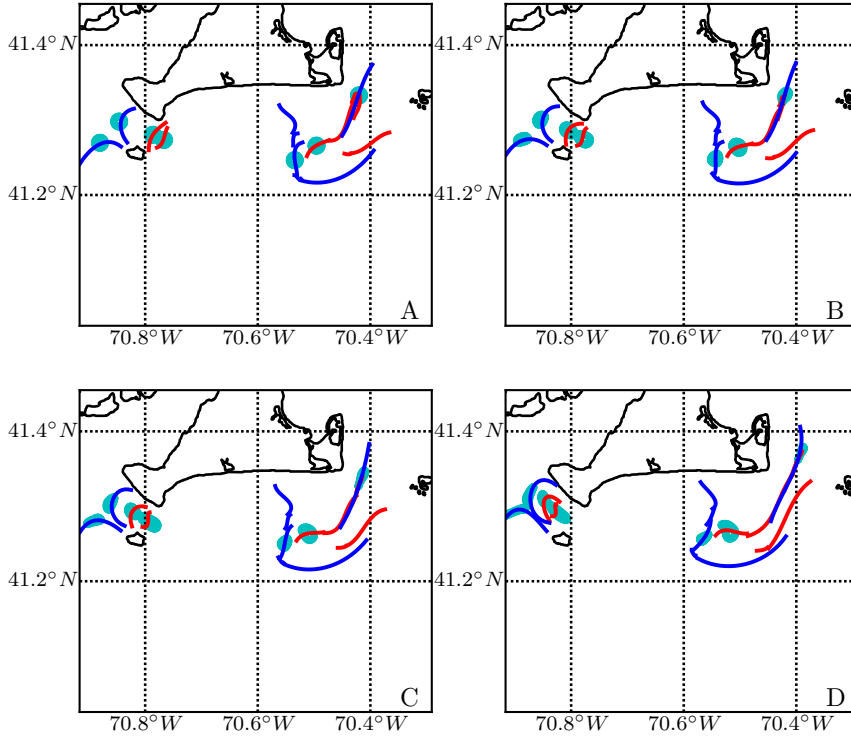


**Fig. 13** iLCSs and passive tracers at different elapsed times,  $t$ . A)  $t - t_0 = 0$  hr, B)  $t - t_0 = 0.5$  hr, C)  $t - t_0 = 1$  hr, D)  $t - t_0 = 2$  hr. Repelling iLCSs are shown in red, attracting iLCSs in blue, and passive tracers in cyan.

The RMSE of Eulerian approximations of the FTLE field, as the flow is integrated backward in time from the initial time  $t_0 = 0$ , is identical to the two-dimensional case, Figure 3.

Example two-dimensional iLCSs for the three-dimensional double-gyre flow are shown in Figures 14 and 15. Figure 14 shows an attracting iLCS (blue), along with a blob of passive tracers (green). Meanwhile, Figure 15 show a repelling iLCS (red), along with blob of tracers (green). In both figures, the first row shows the the initial configuration from two different angles, while the second row shows the configuration after being advected by the flow for a time of 1.25 in non-dimensional units. In Figure 14, one can see that the green blob, starting out as a sphere around a portion of the iLCS, becomes squeezed towards and spread along the iLCS as the two are advected by the flow. In Figure 15, the green blob, starting as a sphere, spreads out and away from the repelling iLCS as they are advected by the flow. These behaviors demonstrate that iLCSs are indeed the instantaneous approximation of traditional LCSs in three dimensions. An animation for the attracting iLCS can be found at

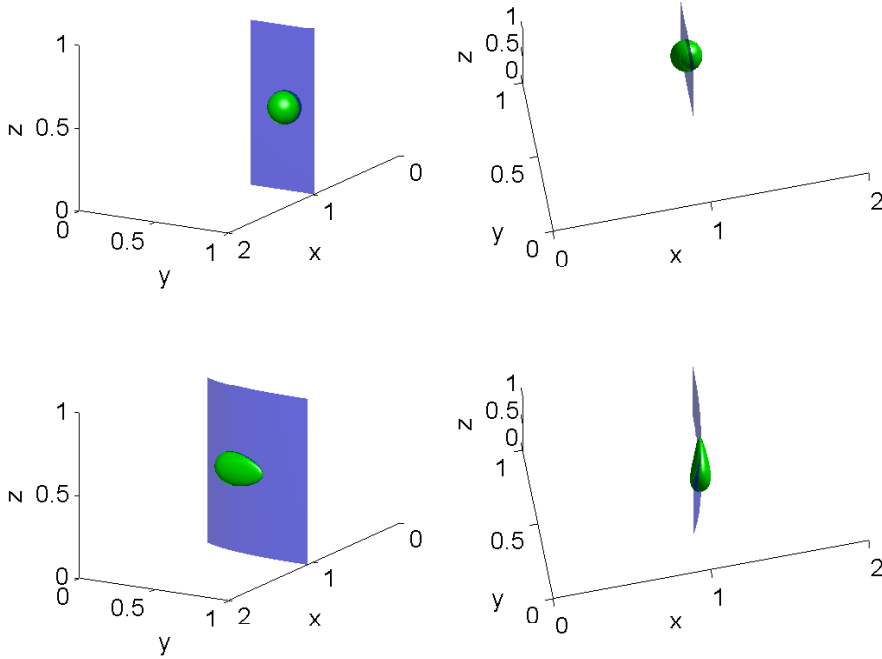


**Fig. 14** An attracting three-dimensional iLCS, blue, with a blob of passive tracers, green, shown from two different viewing angles. Top row shows the iLCS and tracers at the initial time,  $t_0 = 0$ . Bottom row shows the iLCS and tracers after being advected forward in time to  $t = 1.25$ . The animation for the attracting iLCS is at [https://youtu.be/NWxdG7BY0\\_o](https://youtu.be/NWxdG7BY0_o).

[https://youtu.be/NWxdG7BY0\\_o](https://youtu.be/NWxdG7BY0_o), and the repelling iLCS at <https://youtu.be/ZkD3qBnrHLO>.

### 5.6 Three-Dimensional ABC Flow

In this section, iLCSs are applied to a fully coupled three-dimensional flow. Additionally, the convergence of the attraction rate and higher-order approximation to the backward-time FTLE field is demonstrated. For this section, the Arnold-Beltrami-Childress (ABC) flow [79, 80] was chosen, a divergence-free flow commonly used in FTLE and LCS demonstrations. The fluid components of the ABC flow are analytically given by,

$$\begin{aligned}
 \dot{x} &= u = A \sin(z) + C \cos(y), \\
 \dot{y} &= v = B \sin(x) + A \cos(z), \\
 \dot{z} &= w = C \sin(y) + B \cos(x).
 \end{aligned}
 \tag{75}$$

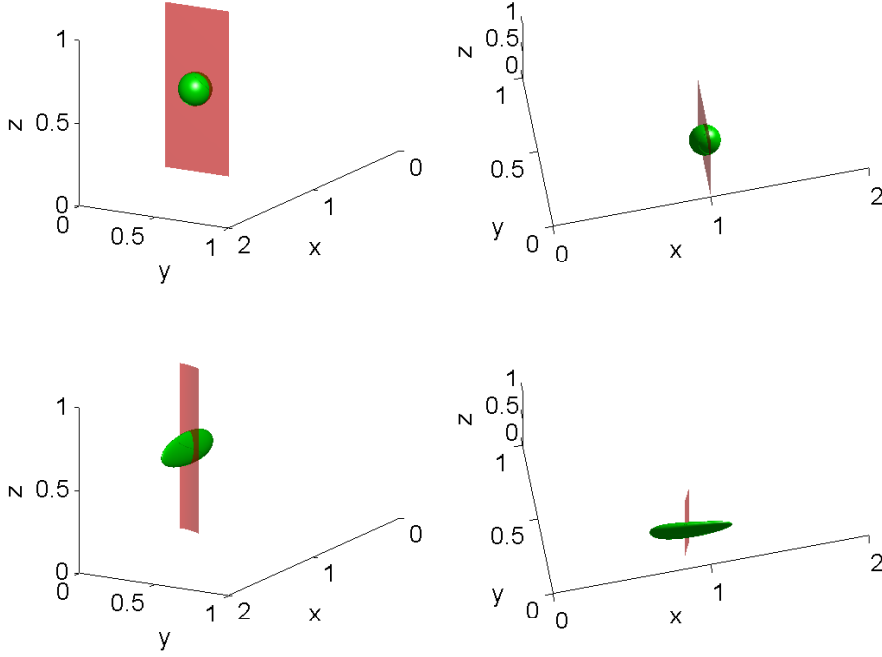


**Fig. 15** A repelling three-dimensional iLCS, red, with a blob of passive tracers, green, from two different viewing angles. Top row shows the iLCS and tracers at the initial time,  $t_0 = 0$ . Bottom row shows the iLCS and tracers after being advected forward in time to  $t = 1.25$ . The animation for the repelling iLCS is at <https://youtu.be/ZkD3qBnrHL0>.

The ABC flow  $\mathbf{v} = (u, v, w)$  is an exact steady solution to Euler's fluid equations and has been shown to have chaotic particle trajectories [80]. The domain for  $\mathbf{x} = (x, y, z)$  is the periodic cube,  $U = [0, 2\pi] \times [0, 2\pi] \times [0, 2\pi]$ . For coefficients,  $A = \sqrt{3}$ ,  $B = \sqrt{2}$ ,  $C = 1$ , were chosen following [81].

As the ABC flow is an analytical flow, it is possible to analytically express the repulsion and attraction rate fields, respectively, as,

$$\begin{aligned} s_3 &= 2\rho^{1/3} \cos\left(\frac{\theta}{3}\right) > 0, \\ s_1 &= -\frac{1}{2}s_3 - \sqrt{3}\rho^{1/3} \sin\left(\frac{\theta}{3}\right) < 0, \end{aligned} \quad (76)$$

where the dependence on position  $\mathbf{x}$  is understood and  $\rho$  and  $\theta$  are given by,

$$\begin{aligned} \rho &= \sqrt{q^2 + |p|}, \\ \theta &= \tan^{-1}\left(\frac{\text{Im}(\sqrt{p})}{q}\right), \end{aligned} \quad (77)$$

where,

$$\begin{aligned}
 q &= -\frac{1}{2}a_0, \\
 p &= \frac{1}{27}a_1^3 + \frac{1}{4}a_0^2, \\
 a_0 &= -\frac{1}{4}(B \cos(x) - C \sin(y))(C \cos(y) - A \sin(z))(-B \sin(x) + A \cos(z)), \\
 a_1 &= -\frac{1}{4} \left[ (B \cos(x) - C \sin(y))^2 \right. \\
 &\quad \left. + (C \cos(y) - A \sin(z))^2 + (-B \sin(x) + A \cos(z))^2 \right]
 \end{aligned} \tag{78}$$

where the coefficients  $a_1$  and  $a_0$  come from the characteristic polynomial for the rate-of-strain tensor  $\mathbf{S}$  for this system,

$$s^3 + a_1 s + a_0 = 0. \tag{79}$$

Figure 16 shows the RMSE of Eulerian approximations with the benchmark FTLE field (computed using the algorithm of [69]) as the flow is integrated backward in time from the initial time  $t_0$ . Since this flow is autonomous,  $t_0$  is

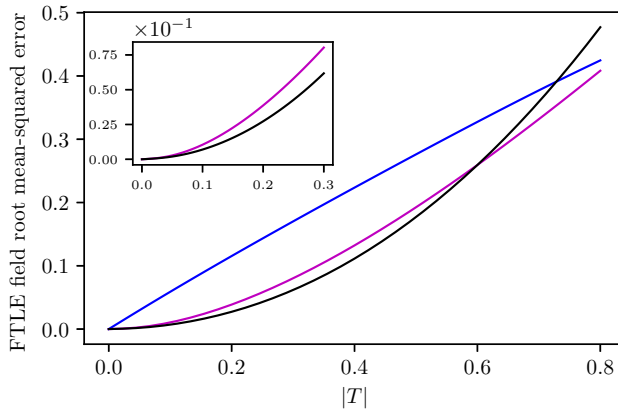


**Fig. 16** RMSE for successive approximations of the backward-time FTLE field for the ABC flow (75) expanded in  $T$ : zeroth-order (blue), first-order (magenta). Time is in non-dimensional units. The inset shows the behavior for the higher order terms for  $|T|$  close to 0.

arbitrary. The RMSE for the attraction rate is shown in blue, the first-order approximation in magenta, and the second-order approximation in black. As in the previous sections, this figure shows that as the integration time goes to zero, the RMSE goes to zero as well.

Figures 17 and 18 examine the efficacy of iLCSs for the ABC flow. As in the previous section, Figure 17 shows an attracting iLCS (blue), along with a blob of passive tracers (green), while Figure 18 show a repelling iLCS (red),

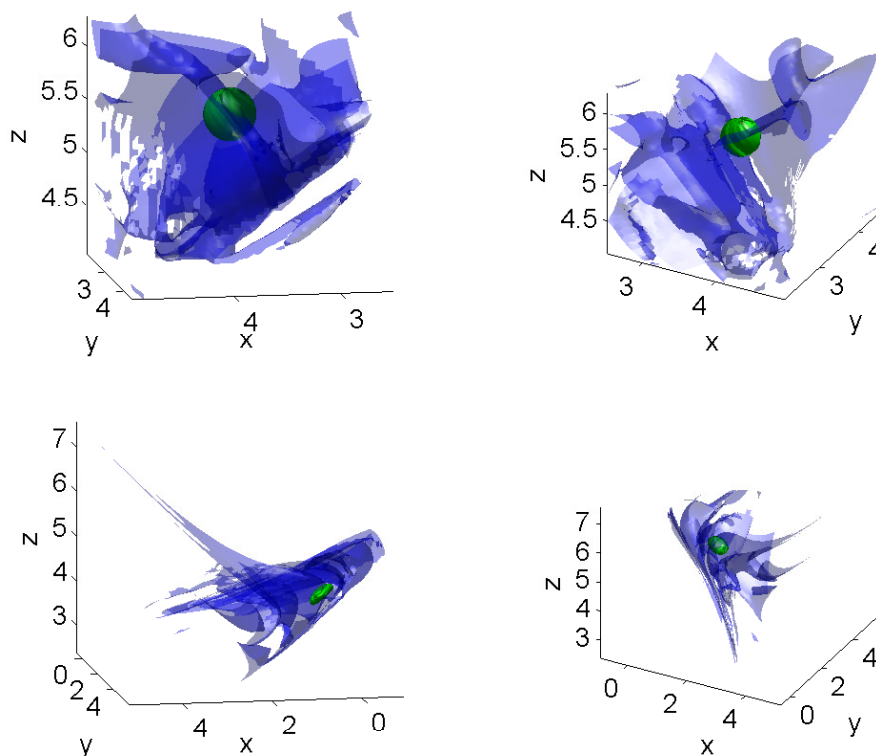


**Fig. 17** An attracting two-dimensional iLCS, blue, within the three-dimensional flow, with a blob of passive tracers, green, shown at different angles. Top row shows the iLCS and tracers at the initial time,  $t_0 = 0$ . Bottom row shows the iLCS and tracers after being advected forward in time to  $t = 1.3$ . An animation of the attracting iLCS and tracer blob is at <https://youtu.be/fmXFcpUEfaI>.

along with two blobs of passive tracers (green). In both figures, the first row shows the initial configuration from two different angles, while the second row shows the configuration after being advected by the flow for a time of 1.3 non-dimensional units. In figure 17, one can see that the green blob, starting out as a sphere around a portion of the iLCS, becomes squeezed towards and spread along the iLCS as the two are advected by the flow. An animation of the attracting iLCS and tracer blob in Figure 17 can be found online at <https://youtu.be/fmXFcpUEfaI>.

Due to the large amounts of twisting and shear in the ABC flow, the repelling effects of iLCS are more difficult to visualize in this flow than in sections 5.3 and 5.5. To compensate for this, two blobs were used in figure 18. The green blobs are initialized above and below a repelling iLCS. In this figure one can see that as the iLCS and tracers are advected by the flow, the tracer blobs are transported away from each other. This also demonstrates

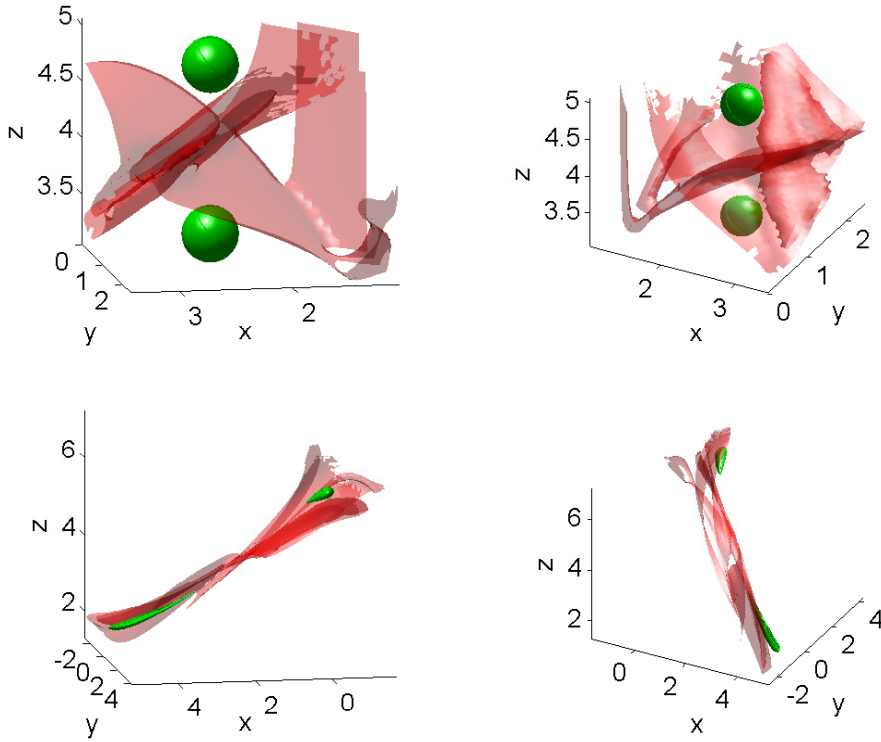


**Fig. 18** A repelling two-dimensional iLCS, red, within the three-dimensional flow, with a blob a passive tracers, green, shown at different angles. Top row shows the iLCS and tracers at the initial time,  $t_0 = 0$ . Bottom row shows the iLCS and tracers after being advected forward in time to  $t = 1.3$ .

the effectiveness of iLCSs as an indicator of flow separatrices, as tracers on opposite sides of the iLCS do not interact with one another.

## 6 Conclusions and Future Directions

This paper has formulated a rigorous mathematical connection between the attraction rate and the backward-time FTLE, as well as the repulsion rate and the forward-time FTLE. It proved that the attraction and repulsion rate fields are the limits of the backward-time and forward-time FTLE fields, respectively, as the integration time,  $T$ , goes to 0. Additionally, it has shown that for small integration times  $|T|$ , the eigenvectors of the right Cauchy-Green strain tensor are equal to those of the Eulerian rate-of-strain tensor. These proofs laid the groundwork for a new Eulerian diagnostic, iLCS, the infinitesimal-time Lagrangian coherent structure, which provide a straightforward approach to identifying the major hyperbolic features dominating particle deformation pat-

terns. These structures can be detected by applying the same ridge detection methods that have been used on the FTLE field to the attraction and repulsion rate fields. Algorithms involving iLCS will be much faster as no particle trajectory integration will be necessary. Moreover, higher-order approximations of the FTLE field using Rivlin-Ericksen tensors were derived and explored. While this study expanded the right Cauchy-Green deformation tensor and FTLE fields, to third order and second order in  $T$ , respectively, one could follow this procedure to arbitrary order  $k$ , assuming the underlying vector field is smooth enough in the sense of differentiability. Automatic differentiation software can be used, such as used for invariant manifold estimation, where expansions up to order  $k = 25$  or higher in the dependent variables have been used [82, 83].

For the example flows considered to illustrate this method, it was found that higher-order FTLE approximations are more accurate for short integration periods, consistent with what would be expected from a Taylor series expansion. For a steady flow with a smooth vector field, such as the nonlinear saddle (51) or the time-independent double-gyre (i.e., (67) with  $\epsilon = 0$ ), the FTLE approximation to order  $k$  in  $T$  will converge to the true FTLE as  $k \rightarrow \infty$  for any  $T$ . This is because there is no effect of unsteadiness, that is, the  $t_0$  dependence of the vector field. The FTLE structure arises merely due to the inhomogeneity of the steady vector field. As a corollary, one could measure the effect of unsteadiness, the  $t_0$  dependence, on the FTLE (and corresponding Lagrangian transport structure) by calculating the difference between a high-order FTLE approximation and the true (particle advection based) FTLE.

The framework presented herein provides a significant contribution to the field of dynamical systems analysis and has important applications in particular for the study of unsteady fluid flows. For example, iLCSs can be used in the place of LCSs when studying environmental or geophysical flows and with considerable computational savings. This study shows that iLCSs are valid predictors of geophysical transport for up to several hours. The use of iLCSs could thus provide a useful diagnostic of the Lagrangian transport structure of these flows more quickly than traditional LCS analysis. This faster analysis would in turn be useful for time sensitive applications, such as search-and-rescue operations [62], hazardous release scenarios [58], or even agricultural applications such as fungicide spraying [22, 29]. Relatedly, Lagrangian diagnostics, such as the FTLE, have recently been used to improve the reduced order models (ROMs) for fluids, such the quasi-geostrophic equations or Navier-Stokes equations [55]. In place of these Lagrangian diagnostics, the higher-order Eulerian diagnostics derived in this paper could be used to improve such ROMs, reducing both the time and the computational power needed generate Lagrangian data-driven ROMs.

Future work on this topic will explore: the existence of lower-dimensional iLCSs embedded within higher-dimensional iLCSs [82, 84–88]; the application of iLCSs and higher-order FTLE approximations to experimental data [51, 68]; the application of higher-order FTLE approximation to ROMs; measures of the influence of unsteadiness compared with inhomogeneity on Lagrangian

transport structure; and the determination of the time interval over which Eulerian diagnostics are most effective.

#### Compliance with ethical standards

**Conflict of interest:** The authors declare that they have no conflict of interest.

**Funding:** This research was supported in part by grants from the National Science Foundation (NSF) under grant numbers AGS 1520825 (Hazards SEES: Advanced Lagrangian Methods for Prediction, Mitigation and Response to Environmental Flow Hazards) and DMS 1821145 (Data-Driven Computation of Lagrangian Transport Structure in Realistic Flows). Any opinions, findings, and conclusions or recommendations expressed in this material are those of the authors and do not necessarily reflect the views of the sponsors.

**Acknowledgements** We thank Hosein Foroutan for providing us with WRF model data, Nicole Abaid for assistance with the perturbation analysis, Gary Nave for fruitful conversations related to some of the ideas covered in this work during their nascent stage, Siavash Ameli for developing and maintaining the TRACE server used for the ocean particle integration calculations, and Pierre Lermusiaux, P.J. Haley, and the MIT-MSEAS team for providing the MSEAS model data.

## Appendices

### A Expansion of the right Cauchy-Green tensor in the integration time

Evaluation of the flow map and therefore the right Cauchy-Green tensor  $\mathbf{C}_{t_0}^t$ , from (5), can be computationally expensive. Therefore, this section seeks an instantaneous approximation that gives the leading order behavior of this tensor field, expanded in terms of the integration time  $T = t - t_0$ .

For tensor fields in what follows, the dependence on  $\mathbf{x}_0$  and  $t_0$  will be notationally dropped for clarity, as it will be understood. For small time  $T$ , the right Cauchy-Green tensor,  $\mathbf{C}$ , may be expanded, as in [67], in terms of the integration time  $T$ ,

$$\mathbf{C} = \mathbf{C}|_{T=0} + \left. \frac{d\mathbf{C}}{dT} \right|_{T=0} T + \frac{1}{2!} \left. \frac{d^2\mathbf{C}}{dT^2} \right|_{T=0} T^2 + \frac{1}{3!} \left. \frac{d^3\mathbf{C}}{dT^3} \right|_{T=0} T^3 + \mathcal{O}(T^4). \quad (80)$$

where the dependence on the initial position and time is understood. Because all derivatives are evaluated at  $T = 0$ ,  $\left. \frac{d}{dt} \right|_{t=t_0} = \left. \frac{d}{dT} \right|_{T=0}$ . The first term on the right denotes the situation of no deformation, therefore,  $\mathbf{C}|_{T=0} = \mathbb{1}$ . The derivatives of the right Cauchy-Green tensor are given by the Rivlin-Ericksen tensors [67, 89],

$$\begin{aligned} \frac{d^k\mathbf{C}}{dt^k} &= \nabla \frac{d\mathbf{x}}{dt} + \left( \nabla \frac{d\mathbf{x}}{dt} \right)^T, & k = 1, \\ \frac{d^k\mathbf{C}}{dt^k} &= \nabla \frac{d^k\mathbf{x}}{dt^k} + \left( \nabla \frac{d^k\mathbf{x}}{dt^k} \right)^T + \sum_{i=1}^{k-1} \binom{k}{i} \left( \nabla \frac{d^i\mathbf{x}}{dt^i} \right)^T \nabla \frac{d^{k-i}\mathbf{x}}{dt^{k-i}}, & k \geq 2. \end{aligned} \quad (81)$$

For small  $|T| \ll 1$ , the leading order behavior is given by the first Rivlin-Ericksen tensor  $(\nabla \mathbf{v} + (\nabla \mathbf{v})^T)$ , which is twice  $\mathbf{S}$ . The second-order term is,

$$\begin{aligned} \frac{d^2 \mathbf{C}}{dt^2} &= \nabla \frac{d^2 \mathbf{x}}{dt^2} + \left( \nabla \frac{d^2 \mathbf{x}}{dt^2} \right)^T + 2 \left( \nabla \frac{d\mathbf{x}}{dt} \right)^T \nabla \frac{d\mathbf{x}}{dt}, \\ &= \nabla \frac{d\mathbf{v}}{dt} + \left( \nabla \frac{d\mathbf{v}}{dt} \right)^T + 2 (\nabla \mathbf{v})^T \nabla \mathbf{v}, \\ &= 2\mathbf{B} \end{aligned} \quad (82)$$

where  $\mathbf{B}$  is the same as given in (13).

The third-order term is

$$\begin{aligned} \frac{d^3 \mathbf{C}}{dt^3} &= \nabla \frac{d^3 \mathbf{x}}{dt^3} + \left( \nabla \frac{d^3 \mathbf{x}}{dt^3} \right)^T + 3 \left[ \left( \nabla \frac{d\mathbf{x}}{dt} \right)^T \nabla \frac{d^2 \mathbf{x}}{dt^2} + \left( \nabla \frac{d^2 \mathbf{x}}{dt^2} \right)^T \nabla \frac{d\mathbf{x}}{dt} \right], \\ &= \nabla \frac{d\mathbf{a}}{dt} + \left( \nabla \frac{d\mathbf{a}}{dt} \right)^T + 3 \left[ (\nabla \mathbf{v})^T \nabla \mathbf{a} + (\nabla \mathbf{a})^T \nabla \mathbf{v} \right], \\ &= 3\mathbf{Q}, \end{aligned} \quad (83)$$

where,

$$\mathbf{Q} \equiv \frac{1}{3} \left[ \nabla \frac{d\mathbf{a}}{dt} + \left( \nabla \frac{d\mathbf{a}}{dt} \right)^T \right] + \left[ (\nabla \mathbf{v})^T \nabla \mathbf{a} + (\nabla \mathbf{a})^T \nabla \mathbf{v} \right]. \quad (84)$$

The expansion of the right Cauchy-Green tensor (80) can be written as,

$$\begin{aligned} \mathbf{C} &= \mathbb{1} + 2T\mathbf{S} + T^2\mathbf{B} + \frac{1}{2}T^3\mathbf{Q} + \mathcal{O}(T^4), \\ &= \mathbb{1} + 2T \left( \mathbf{S} + \frac{1}{2}T\mathbf{B} + \left( \frac{1}{2}T \right)^2 \mathbf{Q} + \mathcal{O}(T^3) \right). \end{aligned} \quad (85)$$

## B Proof of Equation (16)

Let  $\mathbf{A}$  be an  $n \times n$  matrix,  $\lambda$  an eigenvalue of  $\mathbf{A}$ ,  $\boldsymbol{\xi}$  the corresponding eigenvector of  $\mathbf{A}$ ,  $\mathbb{1}$  the  $n \times n$  identity matrix and  $c \in \mathbb{R}$ . By the definition of an eigenvalue  $\mathbf{A}\boldsymbol{\xi} = \lambda\boldsymbol{\xi}$  thus,

$$(\mathbf{A} + c\mathbb{1})\boldsymbol{\xi} = \mathbf{A}\boldsymbol{\xi} + c\boldsymbol{\xi} = \lambda\boldsymbol{\xi} + c\boldsymbol{\xi} = (\lambda + c)\boldsymbol{\xi}. \quad (86)$$

Therefore, if  $\lambda$  is an eigenvalue of  $\mathbf{A}$  with eigenvector  $\boldsymbol{\xi}$ , then  $(\lambda + c)$  is an eigenvalue for  $\mathbf{A} + c\mathbb{1}$  with the same eigenvector  $\boldsymbol{\xi}$ .

### C Eigenvalues of the Taylor-expanded right Cauchy-Green tensor

Let  $\mathbf{S}$  be a real, symmetric  $n \times n$  matrix with  $n$  distinct eigenvalues, and let  $\mathbf{B}$  and  $\mathbf{Q}$  also be real, symmetric  $n \times n$  matrices. Seek the eigenvalues of

$$\mathbf{S}_\varepsilon = \mathbf{S} + \varepsilon\mathbf{B} + \varepsilon^2\mathbf{Q}, \quad (87)$$

a perturbation of  $\mathbf{S}$ , where  $|\varepsilon|$  is a small scalar. In our case of interest, from (85), the small parameter is  $\varepsilon = \frac{1}{2}T$ .

Consider the eigenvalue  $\mu_0$  of  $\mathbf{S}$  with corresponding normalized eigenvector  $\boldsymbol{\xi}_0$ . Let's refer to the perturbed eigenvalue and corresponding perturbed eigenvector of  $\mathbf{S}_\varepsilon$  as  $\mu_\varepsilon$  and  $\boldsymbol{\xi}_\varepsilon$ . one can expand  $\boldsymbol{\xi}_\varepsilon$  and  $\mu_\varepsilon$  in powers of  $\varepsilon$  as

$$\boldsymbol{\xi}_\varepsilon = \boldsymbol{\xi}_0 + \varepsilon\boldsymbol{\xi}_1 + \varepsilon^2\boldsymbol{\xi}_2 + \mathcal{O}(\varepsilon^3), \quad (88)$$

$$\mu_\varepsilon = \mu_0 + \varepsilon\mu_1 + \varepsilon^2\mu_2 + \mathcal{O}(\varepsilon^3). \quad (89)$$

The eigenvector equation  $\mathbf{S}_\varepsilon\boldsymbol{\xi}_\varepsilon = \mu_\varepsilon\boldsymbol{\xi}_\varepsilon$  can be approximated as

$$(\mathbf{S} + \varepsilon\mathbf{B} + \varepsilon^2\mathbf{Q})(\boldsymbol{\xi}_0 + \varepsilon\boldsymbol{\xi}_1 + \varepsilon^2\boldsymbol{\xi}_2) = (\mu_0 + \varepsilon\mu_1 + \varepsilon^2\mu_2)(\boldsymbol{\xi}_0 + \varepsilon\boldsymbol{\xi}_1 + \varepsilon^2\boldsymbol{\xi}_2), \quad (90)$$

which leads to the following three expressions, corresponding to the order one terms, order  $\varepsilon$ , and order  $\varepsilon^2$  terms, respectively,

$$\mathbf{S}\boldsymbol{\xi}_0 = \mu_0\boldsymbol{\xi}_0, \quad (91)$$

$$\mathbf{S}\boldsymbol{\xi}_1 + \mathbf{B}\boldsymbol{\xi}_0 = \mu_0\boldsymbol{\xi}_1 + \mu_1\boldsymbol{\xi}_0, \quad (92)$$

$$\mathbf{S}\boldsymbol{\xi}_2 + \mathbf{B}\boldsymbol{\xi}_1 + \mathbf{Q}\boldsymbol{\xi}_0 = \mu_0\boldsymbol{\xi}_2 + \mu_1\boldsymbol{\xi}_1 + \mu_2\boldsymbol{\xi}_0. \quad (93)$$

Multiply (92) by  $\boldsymbol{\xi}_0^T$  to get,

$$\boldsymbol{\xi}_0^T\mathbf{S}\boldsymbol{\xi}_1 + \boldsymbol{\xi}_0^T\mathbf{B}\boldsymbol{\xi}_0 = \mu_0\boldsymbol{\xi}_0^T\boldsymbol{\xi}_1 + \mu_1\boldsymbol{\xi}_0^T\boldsymbol{\xi}_0, \quad (94)$$

Since  $\boldsymbol{\xi}_0$  is normalized,  $\boldsymbol{\xi}_0^T\boldsymbol{\xi}_0 = 1$ . Also, since  $\mathbf{S}$  is symmetric,

$$\begin{aligned} \boldsymbol{\xi}_0^T\mathbf{S}\boldsymbol{\xi}_1 &= (\boldsymbol{\xi}_1^T\mathbf{S}\boldsymbol{\xi}_0)^T, \\ &= (\boldsymbol{\xi}_1^T\mu_0\boldsymbol{\xi}_0)^T, \\ &= \mu_0\boldsymbol{\xi}_0^T\boldsymbol{\xi}_1, \end{aligned} \quad (95)$$

where (91) was used. Now (94) is,

$$\mu_0\boldsymbol{\xi}_0^T\boldsymbol{\xi}_1 + \boldsymbol{\xi}_0^T\mathbf{B}\boldsymbol{\xi}_0 = \mu_0\boldsymbol{\xi}_0^T\boldsymbol{\xi}_1 + \mu_1, \quad (96)$$

Thus,

$$\mu_1 = \boldsymbol{\xi}_0^T\mathbf{B}\boldsymbol{\xi}_0, \quad (97)$$

which, since  $\mathbf{B}$  is symmetric, represents a quadratic form.

A bound can be put on the term  $\boldsymbol{\xi}_0^T\mathbf{B}\boldsymbol{\xi}_0$ , noting that  $\boldsymbol{\xi}_0$  is a unit vector. If  $b_n$  is the maximum eigenvalue of  $\mathbf{B}$ , then,

$$\max_{\boldsymbol{\xi}_0} \boldsymbol{\xi}_0^T\mathbf{B}\boldsymbol{\xi}_0 = b_n. \quad (98)$$

Similarly, if  $b_1$  is the minimum eigenvalue of  $\mathbf{B}$ , then,

$$\min_{\boldsymbol{\xi}_0} \boldsymbol{\xi}_0^T \mathbf{B} \boldsymbol{\xi}_0 = b_1. \quad (99)$$

So,

$$\mu_1 = \boldsymbol{\xi}_0^T \mathbf{B} \boldsymbol{\xi}_0 \in [b_1, b_n]. \quad (100)$$

So (89) becomes,

$$\mu_\varepsilon = \mu_0 + \varepsilon \mu_1 + \mathcal{O}(\varepsilon^2), \quad (101)$$

where  $\mu_1$  is from (97).

With  $\mu_1$  in hand,  $\boldsymbol{\xi}_1$  can also be determined, which solves the following re-arranged version of (92),

$$(\mathbf{S} - \mu_0 \mathbb{1}) \boldsymbol{\xi}_1 = -(\mathbf{B} - \mu_1 \mathbb{1}) \boldsymbol{\xi}_0. \quad (102)$$

Note that  $(\mathbf{S} - \mu_0 \mathbb{1})$  is not invertible as it has zero determinant, since  $\mu_0$  is an eigenvalue of  $\mathbf{S}$ . The null space of  $(\mathbf{S} - \mu_0 \mathbb{1})$  is  $\text{span}\{\boldsymbol{\xi}_0\}$ . Note that (102) is of the form  $\mathbf{A} \mathbf{x} = \mathbf{b}$  with a square matrix  $\mathbf{A}$  of nullity 1 and a vector  $\mathbf{b}$  which is in the image of  $\mathbf{A}$ , as shown below.

Note that the vector  $\mathbf{B} \boldsymbol{\xi}_0$  can be written as,

$$\mathbf{B} \boldsymbol{\xi}_0 = \mu_1 \boldsymbol{\xi}_0 + d \boldsymbol{\xi}_0'^{\perp}, \quad (103)$$

where  $d \in \mathbb{R}$  and  $\boldsymbol{\xi}_0'^{\perp}$  is, in general, a vector in  $\text{im}(\mathbf{S} - \mu_0 \mathbb{1})$ . Since the coefficient of  $\boldsymbol{\xi}_0$  in (103) is  $\mu_1$  from (97).

The right-hand side of (102) can be written as,

$$-\mathbf{B} \boldsymbol{\xi}_0 + \mu_1 \boldsymbol{\xi}_0 = -d \boldsymbol{\xi}_0'^{\perp}, \quad (104)$$

since the  $\mu_1 \boldsymbol{\xi}_0$  terms cancel. This means the right-hand side of (102) is a vector  $\mathbf{b}$  which is in  $\text{im}(\mathbf{S} - \mu_0 \mathbb{1})$ , the image of the operator on the left-hand side of (102).

One can further determine  $\mu_2$  by multiplying (93) by  $\boldsymbol{\xi}_0^T$  to get, by a similar procedure as before,

$$\mu_0 \boldsymbol{\xi}_0^T \boldsymbol{\xi}_2 + \boldsymbol{\xi}_0^T \mathbf{B} \boldsymbol{\xi}_1 + \boldsymbol{\xi}_0^T \mathbf{Q} \boldsymbol{\xi}_0 = \mu_0 \boldsymbol{\xi}_0^T \boldsymbol{\xi}_2 + \mu_1 \boldsymbol{\xi}_0^T \boldsymbol{\xi}_1 + \mu_2. \quad (105)$$

Thus,

$$\mu_2 = \boldsymbol{\xi}_0^T \mathbf{Q} \boldsymbol{\xi}_0 + \boldsymbol{\xi}_0^T \mathbf{B} \boldsymbol{\xi}_1 - \mu_1 \boldsymbol{\xi}_0^T \boldsymbol{\xi}_1. \quad (106)$$

But take the transpose and,

$$\mu_2 = \boldsymbol{\xi}_0^T \mathbf{Q} \boldsymbol{\xi}_0 + \boldsymbol{\xi}_1^T (\mathbf{B} - \mu_1 \mathbb{1}) \boldsymbol{\xi}_0, \quad (107)$$

$$= \boldsymbol{\xi}_0^T \mathbf{Q} \boldsymbol{\xi}_0 - \boldsymbol{\xi}_1^T (\mathbf{S} - \mu_0 \mathbb{1}) \boldsymbol{\xi}_1, \quad (108)$$

where (102) was used. One can write  $\boldsymbol{\xi}_1$  as,

$$\boldsymbol{\xi}_1 = a \boldsymbol{\xi}_0 + b \boldsymbol{\xi}_0'^{\perp}, \quad (109)$$

where  $a, b \in \mathbb{R}$  and  $\boldsymbol{\xi}_0^\perp \in \text{im}(\mathbf{S} - \mu_0 \mathbb{1})$ , which is, in general, not equal to  $\boldsymbol{\xi}'_0^\perp$ . Hence,

$$\mu_2 = \boldsymbol{\xi}_0^T \mathbf{Q} \boldsymbol{\xi}_0 - b^2 \boldsymbol{\xi}_0^{\perp T} (\mathbf{S} - \mu_0 \mathbb{1}) \boldsymbol{\xi}_0^\perp. \quad (110)$$

Therefore, the only part of  $\boldsymbol{\xi}_1$  which contributes to  $\mu_2$  is the part which is in the image of  $(\mathbf{S} - \mu_0 \mathbb{1})$ .

When dealing with a two-dimensional flow field,  $\text{im}(\mathbf{S} - \mu_0 \mathbb{1})$  is just a 1-dimensional subspace of  $\mathbb{R}^2$ , and thus  $\boldsymbol{\xi}'_0^\perp$  in (104) is parallel to  $\boldsymbol{\xi}_0^\perp$  in (109). Without loss of generality, they can be taken to be equal unit vectors,  $\boldsymbol{\xi}_0^\perp = \boldsymbol{\xi}'_0^\perp$ . Thus, (102) becomes,

$$b(\mathbf{S} - \mu_0 \mathbb{1}) \boldsymbol{\xi}_0^\perp = -d \boldsymbol{\xi}_0^\perp, \quad (111)$$

or,

$$(\mathbf{S} - \mu_0 \mathbb{1}) \boldsymbol{\xi}_0^\perp = -\frac{d}{b} \boldsymbol{\xi}_0^\perp, \quad (112)$$

which is an eigenvector equation for the matrix  $(\mathbf{S} - \mu_0 \mathbb{1})$  with the eigenvector  $\boldsymbol{\xi}_0^\perp$  and corresponding eigenvalue  $\bar{\mu} = -\frac{d}{b}$ , assuming  $b \neq 0$ . Note that if  $b = 0$ , then  $d = 0$ , from (111).

For two-dimensional flows, from  $\boldsymbol{\xi}_0$ , one can obtain  $\boldsymbol{\xi}_0^\perp$  from a 90° counter-clockwise rotation,

$$\boldsymbol{\xi}_0^\perp = \mathbf{R} \boldsymbol{\xi}_0, \quad (113)$$

where,

$$\mathbf{R} = \begin{bmatrix} 0 & -1 \\ 1 & 0 \end{bmatrix}. \quad (114)$$

Now,  $\boldsymbol{\xi}_0^\perp$  was used to obtain  $\bar{\mu}$  from (112) for the case  $d \neq 0$ . With (113) in (112), (112) becomes the following eigenvector equation for  $\mathbf{R}^T (\mathbf{S} - \mu_0 \mathbb{1}) \mathbf{R}$  with eigenvector  $\boldsymbol{\xi}_0$ ,

$$\mathbf{R}^T (\mathbf{S} - \mu_0 \mathbb{1}) \mathbf{R} \boldsymbol{\xi}_0 = \bar{\mu} \boldsymbol{\xi}_0, \quad (115)$$

Therefore  $\bar{\mu}$  is obtained by taking the dot product with  $\boldsymbol{\xi}_0$ ,

$$\bar{\mu} = \boldsymbol{\xi}_0^T \mathbf{R}^T (\mathbf{S} - \mu_0 \mathbb{1}) \mathbf{R} \boldsymbol{\xi}_0, \quad (116)$$

and  $d$  is obtained from (104), noting that  $\boldsymbol{\xi}_0^{\perp T} \boldsymbol{\xi}_0 = 0$ ,

$$\begin{aligned} d &= \boldsymbol{\xi}_0^{\perp T} \mathbf{B} \boldsymbol{\xi}_0, \\ &= \boldsymbol{\xi}_0^T \mathbf{R}^T \mathbf{B} \boldsymbol{\xi}_0. \end{aligned} \quad (117)$$

Thus, (110), for two-dimensional systems, simplifies to,

$$\mu_2 = \begin{cases} \boldsymbol{\xi}_0^T \mathbf{Q} \boldsymbol{\xi}_0, & \text{if } d = 0 \\ \boldsymbol{\xi}_0^T \mathbf{Q} \boldsymbol{\xi}_0 - \frac{d^2}{\bar{\mu}}, & \text{if } d \neq 0 \end{cases} \quad (118)$$

where  $d$  and  $\bar{\mu}$  are from (117) and (116), respectively.

## D Details for Time-Varying Double-Gyre Example

The acceleration field,  $\mathbf{a} = \frac{d}{dt} \mathbf{v} = (a_x, a_y)$ , for the double-gyre, (67), is given by,

$$\begin{aligned} a_x &= -\pi^2 A \cos(\pi f) \cos(\pi y) \frac{\partial f}{\partial t} + \frac{1}{2} \pi^3 A^2 \sin(2\pi f) \frac{\partial f}{\partial x}, \\ a_y &= \pi^2 A \left[ -\sin(\pi f) \sin(\pi y) \frac{\partial f}{\partial x} \frac{\partial f}{\partial t} + \frac{1}{\pi} \cos(\pi f) \sin(\pi y) \frac{\partial^2 f}{\partial x \partial t} \right] \\ &\quad + \frac{1}{2} \pi^3 A^2 \sin(2\pi y) \left[ \sin^2(\pi f) \frac{\partial f}{\partial x} + \cos^2(\pi f) \left( \frac{\partial f}{\partial x} \right)^2 - \frac{1}{2\pi} \sin(2\pi f) \frac{\partial^2 f}{\partial x^2} \right], \end{aligned} \quad (119)$$

where the dependence of the function  $f$ , from (66), is understood.

The components of the symmetric  $\mathbf{B}$  matrix are,

$$\begin{aligned} B_{xx} &= -A\pi^2 \cos(\pi f) \cos(\pi y) \frac{\partial^2 f}{\partial x \partial t} + \frac{1}{2} A\pi^3 \sin(2\pi f) \frac{\partial f}{\partial x} \frac{\partial f}{\partial t} \\ &\quad + A^2 \pi^3 \sin(2\pi f) \frac{\partial^2 f}{\partial x^2} \left( \frac{1}{2} - \sin^2(\pi y) \left( \frac{\partial f}{\partial x} \right)^2 \right) + A^2 \pi^4 \cos(2\pi f) \left( \frac{\partial f}{\partial x} \right)^2 \\ &\quad + A^2 \pi^4 \sin^2(\pi f) \sin^2(\pi y) \left( \frac{\partial f}{\partial x} \right)^4 + A^2 \pi^2 \cos^2(\pi f) \sin^2(\pi y) \frac{\partial^2 f}{\partial x^2} \\ &\quad + A^2 \pi^4 \cos^2(\pi f) \cos^2(\pi y) \left( \frac{\partial f}{\partial x} \right)^2, \end{aligned} \quad (120)$$

$$\begin{aligned} B_{xy} &= \frac{1}{2} A\pi \cos(\pi f) \sin(\pi y) \left[ \frac{\partial^3 f}{\partial x^2 \partial t} + \pi^2 \left( 1 - \left( \frac{\partial f}{\partial x} \right)^2 \right) \right] \\ &\quad - A\pi^2 \sin(\pi f) \sin(\pi y) \left( \frac{\partial f}{\partial x} \frac{\partial^2 f}{\partial x \partial t} - \frac{1}{2} \frac{\partial^2 f}{\partial x^2} \frac{\partial f}{\partial t} \right) \\ &\quad - \frac{1}{4} A^2 \pi^4 \sin(2\pi f) \sin(2\pi y) \left[ \frac{\partial f}{\partial x} \left( 1 + \left( \frac{\partial f}{\partial x} \right)^2 \right) + \frac{1}{2} \frac{\partial^3 f}{\partial x^3} \right], \end{aligned} \quad (121)$$

$$\begin{aligned} B_{yy} &= A\pi^2 \cos(\pi f) \cos(\pi y) \frac{\partial^2 f}{\partial x \partial t} - A\pi^3 \sin(\pi f) \cos(\pi y) \frac{\partial f}{\partial x} \frac{\partial f}{\partial t} \\ &\quad - \frac{1}{2} A^2 \pi^3 \sin(2\pi f) \sin(2\pi y) \frac{\partial^2 f}{\partial x^2} \\ &\quad + A^2 \pi^4 \cos^2(\pi f) \cos^2(\pi y) \left( \frac{\partial f}{\partial x} \right)^2 + A^2 \pi^4 \sin^2(\pi f) \sin^2(\pi y) \\ &\quad + A^2 \pi^4 \left( \frac{\partial f}{\partial x} \right)^2 \left( \cos^2(\pi f) - \sin^2(\pi y) \right). \end{aligned} \quad (122)$$

The normalized eigenvector of  $\mathbf{S}(\mathbf{x}_0, t_0)$  corresponding to the eigenvalue  $s_1(\mathbf{x}_0, t_0)$  given in (69) is,

$$\boldsymbol{\xi}_{s_1} = \begin{bmatrix} \xi_x \\ \xi_y \end{bmatrix} = \frac{1}{N} \begin{bmatrix} \frac{1}{2} \alpha \\ \bar{s}_1 + \beta \end{bmatrix}, \quad (123)$$

where,

$$\begin{aligned} \bar{s}_1 &= \frac{s_1}{\pi^2 A} = -\frac{1}{2} \sqrt{\alpha^2 + 4\beta^2}, \\ N &= \sqrt{\frac{1}{4} \alpha^2 + (\bar{s}_1 + \beta)^2}, \\ \alpha &= \sin(\pi f) \sin(\pi y) \left( 1 - \frac{\partial f}{\partial x} \right) + \frac{1}{\pi} \cos(\pi f) \sin(\pi y) \frac{\partial^2 f}{\partial x^2}, \\ \beta &= \cos(\pi f) \cos(\pi y) \frac{\partial f}{\partial x}. \end{aligned} \quad (124)$$

The coefficient of  $T$  in the approximation of the backward-time FTLE for the double-gyre is thus given by  $s_1^2 - \frac{1}{2}\boldsymbol{\xi}_{s_1}^T \mathbf{B}\boldsymbol{\xi}_{s_1}$  which can be expressed as,

$$a(\mathbf{x}_0, t_0) = s_1^2 - \frac{1}{2}(B_{xx}\xi_x^2 + 2B_{xy}\xi_x\xi_y + B_{yy}\xi_y^2), \quad (125)$$

using the above formulas. This yields a backward-time FTLE approximation for small backward times  $T < 0$  of,

$$\sigma_{t_0}^{t_0+T}(\mathbf{x}_0) = s_1(\mathbf{x}_0, t_0) + a(\mathbf{x}_0, t_0)T + \mathcal{O}(T^2). \quad (126)$$

Note that the first and second terms have explicit dependence on both initial position and initial time.

## References

1. Shadden, S. C., Lekien, F. and Marsden, J. E. [2005] Definition and properties of Lagrangian coherent structures from finite-time Lyapunov exponents in two-dimensional aperiodic flows. *Physica D: Nonlinear Phenomena* **212**(3):271–304.
2. Lekien, F., Shadden, S. C. and Marsden, J. E. [2007] Lagrangian coherent structures in n-dimensional systems. *Journal of Mathematical Physics* **48**(6):065404.
3. Gawlik, E. S., Marsden, J. E., Du Toit, P. C. and Campagnola, S. [2009] Lagrangian coherent structures in the planar elliptic restricted three-body problem. *Celestial Mechanics and Dynamical Astronomy* **103**(3):227–249.
4. Lekien, F. and Ross, S. D. [2010] The computation of finite-time Lyapunov exponents on unstructured meshes and for non-Euclidean manifolds. *Chaos: An Interdisciplinary Journal of Nonlinear Science* **20**(1):017505.
5. Brunton, S. L. and Rowley, C. W. [2010] Fast computation of FTLE fields for unsteady flows: a comparison of methods. *Chaos: An Interdisciplinary Journal of Nonlinear Science* **20**(1):017503.
6. Mendoza, C. and Mancho, A. M. [2010] Hidden geometry of ocean flows. *Physical Review Letters* **105**(3):038501.
7. Lipinski, D. and Mohseni, K. [2010] A ridge tracking algorithm and error estimate for efficient computation of Lagrangian coherent structures. *Chaos: An Interdisciplinary Journal of Nonlinear Science* **20**(1):017504.
8. Ross, S. D., Tanaka, M. L. and Senatore, C. [2010] Detecting dynamical boundaries from kinematic data in biomechanics. *Chaos: An Interdisciplinary Journal of Nonlinear Science* **20**(1):017507.
9. Senatore, C. and Ross, S. D. [2011] Detection and characterization of transport barriers in complex flows via ridge extraction of the finite time Lyapunov exponent field. *International Journal for Numerical Methods in Engineering* **86**(9):1163–1174.
10. Schwartz, I. B., Forgoston, E., Bianco, S. and Shaw, L. B. [2011] Converging towards the optimal path to extinction. *Journal of The Royal Society Interface* **8**(65):1699–1707.

11. Leung, S. [2011] An Eulerian approach for computing the finite time Lyapunov exponent. *Journal of Computational Physics* **230**(9):3500–3524.
12. Haller, G. [2011] A variational theory of hyperbolic Lagrangian coherent structures. *Physica D: Nonlinear Phenomena* **240**(7):574–598.
13. Tallapragada, P., Ross, S. D. and Schmale III, D. G. [2011] Lagrangian coherent structures are associated with fluctuations in airborne microbial populations. *Chaos: An Interdisciplinary Journal of Nonlinear Science* **21**:033122.
14. Schindler, B., Peikert, R., Fuchs, R. and Theisel, H. [2012] Ridge concepts for the visualization of Lagrangian coherent structures. *Topological Methods in Data Analysis and Visualization II* 221–235.
15. Schindler, B., Fuchs, R., Barp, S., Waser, J., Pobitzer, A., Carnecky, R., Matković, K. and Peikert, R. [2012] Lagrangian coherent structures for design analysis of revolving doors. *IEEE Transactions on Visualization and Computer Graphics* **18**(12):2159–2168.
16. Peng, J. and Peterson, R. [2012] Attracting structures in volcanic ash transport. *Atmospheric Environment* **48**:230–239.
17. Tallapragada, P. and Ross, S. D. [2013] A set oriented definition of finite-time Lyapunov exponents and coherent sets. *Communications in Nonlinear Science and Numerical Simulation* **18**(5):1106–1126.
18. BozorgMagham, A. E., Ross, S. D. and Schmale III, D. G. [2013] Real-time prediction of atmospheric Lagrangian coherent structures based on forecast data: An application and error analysis. *Physica D: Nonlinear Phenomena* **258**:47–60.
19. Michini, M., Hsieh, M. A., Forgoston, E. and Schwartz, I. B. [2014] Robotic tracking of coherent structures in flows. *IEEE Transactions on Robotics* **30**(3):593–603.
20. Garaboa-Paz, D., Eiras-Barca, J., Huhn, F. and Pérez-Muñuzuri, V. [2015] Lagrangian coherent structures along atmospheric rivers. *Chaos: An Interdisciplinary Journal of Nonlinear Science* **25**(6):063105.
21. BozorgMagham, A. E. and Ross, S. D. [2015] Atmospheric Lagrangian coherent structures considering unresolved turbulence and forecast uncertainty. *Communications in Nonlinear Science and Numerical Simulation* **22**(1):964–979.
22. Schmale III, D. G. and Ross, S. D. [2015] Highways in the sky: scales of atmospheric transport of plant pathogens. *Annual Review of Phytopathology* **53**:591–611.
23. BozorgMagham, A. E., Ross, S. D. and Schmale III, D. G. [2015] Local finite-time Lyapunov exponent, local sampling and probabilistic source and destination regions. *Nonlinear Processes in Geophysics* **22**(6):663–677.
24. Haller, G. [2015] Lagrangian coherent structures. *Annual Review of Fluid Mechanics* **47**(1):137–162.
25. Mease, K., Topcu, U., Aykutluğ, E. and Maggia, M. [2016] Characterizing two-timescale nonlinear dynamics using finite-time Lyapunov exponents and subspaces. *Communications in Nonlinear Science and Numerical Sim-*

- ulation **36**:148–174.
26. Hadjighasem, A., Farazmand, M., Blazeovski, D., Froyland, G. and Haller, G. [2017] A critical comparison of Lagrangian methods for coherent structure detection. *Chaos: An Interdisciplinary Journal of Nonlinear Science* **27**(5):053104.
  27. Onozaki, K., Yoshimura, H. and Ross, S. D. [2017] Tube dynamics and low energy Earth–Moon transfers in the 4-body system. *Advances in Space Research* **60**(10):2117–2132.
  28. Garaboa-Paz, D., Nieves, L. and Pérez-Muñuzuri, V. [2017] Influence of finite-time Lyapunov exponents on winter precipitation over the Iberian Peninsula. *Nonlinear Processes in Geophysics* **24**(2):227.
  29. Schmale III, D. G. and Ross, S. D. [2017] High-flying microbes: Aerial drones and chaos theory help researchers explore the many ways that microorganisms spread havoc around the world. *Scientific American* **2**:32–37.
  30. You, G., Wong, T. and Leung, S. [2017] Eulerian methods for visualizing continuous dynamical systems using Lyapunov exponents. *SIAM Journal on Scientific Computing* **39**(2):A415–A437.
  31. Chang, H., Huntley, H. S., Kirwan Jr, A., Lipphardt Jr, B. and Sulman, M. H. [2018] Transport structures in a 3D periodic flow. *Communications in Nonlinear Science and Numerical Simulation* **61**:84–103.
  32. Liu, Y., Wilson, C., Green, M. A. and Hughes, C. W. [2018] Gulf Stream Transport and Mixing Processes via Coherent Structure Dynamics. *Journal of Geophysical Research: Oceans* **123**(4):3014–3037.
  33. Hsieh, M. A., Hajieghrary, H., Kularatne, D., Heckman, C. R., Forgo-ton, E., Schwartz, I. B. and Yecko, P. A. [2018] Small and adrift with self-control: using the environment to improve autonomy. In *Robotics Research*, 387–402. Springer.
  34. Balasuriya, S., Ouellette, N. T. and Rypina, I. I. [2018] Generalized Lagrangian coherent structures. *Physica D: Nonlinear Phenomena* **372**:31–51.
  35. Shadden, S. C., Dabiri, J. O. and Marsden, J. E. [2006] Lagrangian analysis of fluid transport in empirical vortex ring flows. *Physics of Fluids* **18**(4):047105.
  36. Olcay, A. B., Pottebaum, T. S. and Krueger, P. S. [2010] Sensitivity of Lagrangian coherent structure identification to flow field resolution and random errors. *Chaos* **20**(1):017506.
  37. Raben, S. G., Ross, S. D. and Vlachos, P. P. [2014] Computation of finite-time Lyapunov exponents from time-resolved particle image velocimetry data. *Experiments in Fluids* **55**(1):1638.
  38. Raben, S. G., Ross, S. D. and Vlachos, P. P. [2014] Experimental determination of three-dimensional finite-time Lyapunov exponents in multi-component flows. *Experiments in Fluids* **55**(10):1824.
  39. Tanaka, M. L. and Ross, S. D. [2009] Separatrices and basins of stability from time series data: an application to biodynamics. *Nonlinear Dynamics* **58**(1-2):1–21.

40. Tanaka, M. L., Nussbaum, M. A. and Ross, S. D. [2009] Evaluation of the threshold of stability for the human spine. *Journal of biomechanics* **42**(8):1017–1022.
41. Tanaka, M. L., Ross, S. D. and Nussbaum, M. A. [2010] Mathematical modeling and simulation of seated stability. *Journal of biomechanics* **43**(5):906–912.
42. Shadden, S. C. and Taylor, C. A. [2008] Characterization of coherent structures in the cardiovascular system. *Annals of Biomedical Engineering* **36**(7):1152–1162.
43. Shadden, S. C., Astorino, M. and Gerbeau, J.-F. [2010] Computational analysis of an aortic valve jet with Lagrangian coherent structures. *Chaos: An Interdisciplinary Journal of Nonlinear Science* **20**(1):017512.
44. Töger, J., Kanski, M., Carlsson, M., Kovács, S. J., Söderlind, G., Arheden, H. and Heiberg, E. [2012] Vortex ring formation in the left ventricle of the heart: analysis by 4D flow MRI and Lagrangian coherent structures. *Annals of Biomedical Engineering* **40**(12):2652–2662.
45. Shadden, S. C. and Arzani, A. [2015] Lagrangian postprocessing of computational hemodynamics. *Annals of Biomedical Engineering* **43**(1):41–58.
46. Arzani, A., Gambaruto, A. M., Chen, G. and Shadden, S. C. [2017] Wall shear stress exposure time: a Lagrangian measure of near-wall stagnation and concentration in cardiovascular flows. *Biomechanics and Modeling in Mechanobiology* **16**(3):787–803.
47. Shadden, S. C., Lekien, F., Paduan, J. D., Chavez, F. P. and Marsden, J. E. [2009] The correlation between surface drifters and coherent structures based on high-frequency radar data in Monterey Bay. *Deep Sea Research Part II: Topical Studies in Oceanography* **56**(3-5):161–172.
48. Rypina, I. I., Pratt, L. J. and Lozier, M. S. [2011] Near-surface transport pathways in the North Atlantic Ocean: Looking for throughput from the subtropical to the subpolar gyre. *Journal of Physical Oceanography* **41**(5):911–925.
49. Kirincich, A. [2016] Remote sensing of the surface wind field over the coastal ocean via direct calibration of HF radar backscatter power. *Journal of Atmospheric and Oceanic Technology* **33**(7):1377–1392.
50. D’Asaro, E. A., Shcherbina, A. Y., Klymak, J. M., Molemaker, J., Novelli, G., Guigand, C. M., Haza, A. C., Haus, B. K., Ryan, E. H., Jacobs, G. A., Huntley, H. S., Laxague, N. J. M., Chen, S., Judt, F., McWilliams, J. C., Barkan, R., Kirwan, A. D., Poje, A. C. and Özgökmen, T. M. [2018] Ocean convergence and the dispersion of flotsam. *Proceedings of the National Academy of Sciences* **115**(6):1162–1167. URL <https://www.pnas.org/content/115/6/1162>.
51. Nolan, P. J., Pinto, J., González-Rocha, J., Jensen, A., Vezzi, C., Bailey, S., de Boer, G., Diehl, C., Laurence, R., Powers, C., Ross, S. D. and Schmale III, D. G. [2018] Coordinated unmanned aircraft system (UAS) and ground-based weather measurements to predict Lagrangian coherent structures (LCSs). *Sensors* **18**(12):4448.

52. González-Rocha, J., Woolsey, C. A., Sultan, C. and De Wekker, S. F. J. [2018] Sensing Wind from Quadrotor Motion. *Journal of Guidance, Control, and Dynamics* DOI: 10.2514/1.G003542.
53. Van Dop, H., Addis, R., Fraser, G., Girardi, F., Graziani, G., Inoue, Y., Kelly, N., Klug, W., Kulmala, A., Nodop, K. and Pretel, J. [1998] ETEX: A European tracer experiment; observations, dispersion modelling and emergency response. *Atmospheric Environment* **32**(24):4089–4094.
54. De Dominicis, M., Falchetti, S., Trotta, F., Pinardi, N., Giacomelli, L., Napolitano, E., Fazioli, L., Sorgente, R., Haley Jr, P. J., Lermusiaux, P. F., Martins, F. and Cocco, M. [2014] A relocatable ocean model in support of environmental emergencies. *Ocean Dynamics* **64**(5):667–688.
55. Xie, X., Nolan, P. J., Ross, S. D. and Iliescu, T. [2019]. Lagrangian data-driven reduced order modeling of finite time Lyapunov exponents. <https://arxiv.org/abs/1808.05635>.
56. Buesseler, K. O., Jayne, S. R., Fisher, N. S., Rypina, I. I., Baumann, H., Baumann, Z., Breier, C. F., Douglass, E. M., George, J., Macdonald, A. M. et al. [2012] Fukushima-derived radionuclides in the ocean and biota off Japan. *Proceedings of the National Academy of Sciences* **109**(16):5984–5988.
57. Mezić, I., Loire, S., Fonoberov, V. A. and Hogan, P. [2010] A new mixing diagnostic and Gulf oil spill movement. *Science* **330**(6003):486–489.
58. Olascoaga, M. J. and Haller, G. [2012] Forecasting sudden changes in environmental pollution patterns. *Proceedings of the National Academy of Sciences* **109**(13):4738–4743.
59. García-Garrido, V., Ramos, A., Mancho, A., Coca, J. and Wiggins, S. [2016] A dynamical systems perspective for a real-time response to a marine oil spill. *Marine Pollution Bulletin* **112**(1-2):201–210.
60. Allshouse, M. R., Ivey, G. N., Lowe, R. J., Jones, N. L., Beegle-Krause, C., Xu, J. and Peacock, T. [2017] Impact of windage on ocean surface Lagrangian coherent structures. *Environmental Fluid Mechanics* **17**(3):473–483.
61. Breivik, Ø., Allen, A. A., Maisondieu, C. and Roth, J. C. [2011] Wind-induced drift of objects at sea: The leeway field method. *Applied Ocean Research* **33**(2):100–109.
62. Peacock, T. and Haller, G. [2013] Lagrangian coherent structures: The hidden skeleton of fluid flows. *Physics Today* **66**(2):41.
63. Draxler, R. R. and Hess, G. [1998] An overview of the HYSPLIT\_4 modelling system for trajectories. *Australian Meteorological Magazine* **47**(4):295–308.
64. Rypina, I. I., Kirincich, A. R., Limeburner, R. and Udovydchenkov, I. A. [2014] Eulerian and Lagrangian correspondence of high-frequency radar and surface drifter data: Effects of radar resolution and flow components. *Journal of Atmospheric and Oceanic Technology* **31**(4):945–966.
65. Ameli, S. and Shadden, S. C. [2019] A transport method for restoring incomplete ocean current measurements. *Journal of Geophysical Research: Oceans* **124**(1):227–242.

66. Serra, M. and Haller, G. [2016] Objective Eulerian coherent structures. *Chaos: An Interdisciplinary Journal of Nonlinear Science* **26**(5):053110.
67. Nave Jr, G. K., Nolan, P. J. and Ross, S. D. [2019] Trajectory-free approximation of phase space structures using the trajectory divergence rate. *Nonlinear Dynamics* .
68. Nolan, P. J., McClelland, H. G., Woolsey, C. A. and Ross, S. D. [2019] A method for detecting atmospheric Lagrangian coherent structures using a single fixed-wind unmanned aircraft system. *Sensors* **19**(7):1607.
69. Du Toit, P. C. and Marsden, J. E. [2010] Horseshoes in hurricanes. *Journal of Fixed Point Theory and Applications* **7**(2):351–384.
70. Ameli, S., Desai, Y. and Shadden, S. C. [2014] Development of an efficient and flexible pipeline for Lagrangian coherent structure computation. In *Topological Methods in Data Analysis and Visualization III*, 201–215. Springer.
71. Rypina, I. I., Scott, S., Pratt, L. J. and Brown, M. G. [2011] Investigating the connection between complexity of isolated trajectories and Lagrangian coherent structures .
72. Pratt, L. J., Rypina, I. I., Özgökmen, T. M., Wang, P., Childs, H. and Bebieva, Y. [2014] Chaotic advection in a steady, three-dimensional, Ekman-driven eddy. *J. Fluid Mech.* **738**:143–183.
73. Pérez-Munuzuri, V. and Huhn, F. [2013] Path-integrated Lagrangian measures from the velocity gradient tensor. *Nonlinear Processes in Geophysics* **20**(6):987–991.
74. Peikert, R., Schindler, B. and Carnecky, R. [2012] Ridge surface methods for the visualization of Lagrangian coherent structures. In *Proceedings of the Ninth International Conference on Flow Dynamics, Sendai, Japan*, 206–207.
75. Weather Research and Forecasting Model. <https://www.mmm.ucar.edu/weather-research-and-forecasting-model>. Accessed: 2019-02-02.
76. Schmale, D. G., Ross, S. D., Feters, T. L., Tallapragada, P., Wood-Jones, A. K. and Dingus, B. [2012] Isolates of *Fusarium graminearum* collected 40–320 meters above ground level cause *Fusarium* head blight in wheat and produce trichothecene mycotoxins. *Aerobiologia* **28**(1):1–11.
77. Barbieri, L. K., Kral, S. T., Bailey, S. C. C., Frazier, A. E., Jacob, J. D., D. Brus, P. B. C., Crick, C., Elston, J., Foroutan, H., González-Rocha, J., Greene, B. R., Guzman, M. I., Houston, A. L., Islam, A., Kemppinen, O., Pillar-Little, E. A., Reuder, J., Ross, S. D., Sama, M., Schmale III, D. G., Schuyler, T. J., Smith, S., Waugh, S., Doddi, A., Lawrence, D., Dixon, C., Borenstein, S. and de Boer, G. [2019] Small Unmanned Aircraft Systems (sUAS) in Atmospheric Science: Measurement Intercomparison for LAPSE-RATE. *Sensors* .
78. Haley, P. J. and Lermusiaux, P. F. [2010] Multiscale two-way embedding schemes for free-surface primitive equations in the “Multidisciplinary Simulation, Estimation and Assimilation System”. *Ocean Dynamics* **60**(6):1497–1537.

79. Arnold, V. I. [2014] *Sur la topologie des écoulements stationnaires des fluides parfaits*, 15–18. Springer Berlin Heidelberg, Berlin, Heidelberg.
80. Dombre, T., Frisch, U., Greene, J. M., Hénon, M., Mehr, A. and Soward, A. M. [1986] Chaotic streamlines in the ABC flows. *Journal of Fluid Mechanics* **167**:353–391.
81. Henon, M. [1966] Sur la topologie des lignes de courant dans un cas particulier. *Comptes Rendus Acad. Sci. Paris A* **262**:312–314.
82. Gómez, G., Koon, W. S., Lo, M. W., Marsden, J. E., Masdemont, J. and Ross, S. D. [2004] Connecting orbits and invariant manifolds in the spatial restricted three-body problem. *Nonlinearity* **17**(5):1571.
83. Farrés, A. and Jorba, A. [2010] On the high order approximation of the centre manifold for ODEs. *Discrete Contin. Dyn. Syst. Ser. B* **14**(3):977–1000.
84. Nave Jr, G. K. and Ross, S. D. [2019] Global phase space structures in a model of passive descent. *Communications in Nonlinear Science and Numerical Simulation* .
85. Doedel, E. J., Krauskopf, B. and Osinga, H. M. [2015] Global organization of phase space in the transition to chaos in the Lorenz system. *Nonlinearity* **28**(11):R113–R139.
86. Gabern, F., Koon, W. S., Marsden, J. E. and Ross, S. D. [2005] Theory and computation of non-RRKM lifetime distributions and rates in chemical systems with three or more degrees of freedom. *Physica D: Nonlinear Phenomena* **211**(3-4):391–406.
87. Surana, A., Jacobs, G. B., Grunberg, O. and Haller, G. [2008] An exact theory of three-dimensional fixed separation in unsteady flows. *Physics of Fluids* **20**(10):107101.
88. Ross, S. D., BozorgMagham, A. E., Naik, S. and Virgin, L. N. [2018] Experimental validation of phase space conduits of transition between potential wells. *Physical Review E* **98**(5):052214.
89. Truesdell, C. and Noll, W. [2004] *The Non-Linear Field Theories of Mechanics*. Springer.